CrossMark

Critical aspects of impedance spectroscopy in silicon solar cell characterization: A review

Pankaj Yadav[a,*], Kavita Pandey[b], Vishwa Bhatt[b], Manoj Kumar[c,*], Joondong Kim[a]

[a] Department of Electrical Engineering, Incheon National University, Incheon 406772, Republic of Korea
[b] School of Solar Energy, Pandit Deendayal Petroleum University, Gandhinagar 382007, India
[c] School of Technology, Pandit Deendayal Petroleum University, Gandhinagar 382007, India

ABSTRACT

Solar energy generation and utilization is dominated by silicon based solar photovoltaic technology, which has a market share of 80–90% of the solar photovoltaic industry worldwide. The performance indicating parameters of silicon solar cells include power conversion efficiency, series and shunt resistance, ideality factor and built-in potential. These parameters are mostly characterized by DC techniques, which is limited by its insufficiency to identify other important parameters such as interfacial diffusion and transition capacitance and resistive and capacitive components of p-p$^+$ interface of a silicon solar cell. Impedance spectroscopy is considered to be one of the most promising techniques for the characterization of abovementioned performance limiting parameters of a solar cell. In order to address the decoupling of various physical processes associated with different interfaces of a solar cell, quantitative analysis of the impedance spectroscopic data is required. An appropriate mathematical model is frequently used to correlate with the physical performance limiting parameters. This review presents a complete overview of the required mathematical models to analyse impedance spectroscopic data for interfacial processes of silicon solar cell.

1. Introduction

In recent years, critical environmental issues have increased the awareness to reduce the global warming and climate change [1]. In this effort many countries and research laboratories around the world actively promote the renewable energy applications. Among the various sources of renewable energy, the utilization of solar energy through photovoltaic (PV) cells has emerged as a promising source of green energy [2]. Silicon (Si) based PV module technology has a maximum market share of 80–90% of the PV cells manufactured worldwide [3]. The continuous research and development in the field of silicon solar cells has introduced novel design and concepts, new materials & processing methods and cost strategies [4–6] to reduce the cost of silicon based PV modules.

The performance indicating parameters of these solar cells includes power conversion efficiency (η), series and shunt resistance, ideality factor, and built in potential. The values of these parameters are calculated by using the DC current – voltage characterization techniques that dictates the material properties of the cell [7–10]. By exploring the aforementioned parameters as a function of forward bias (FB), reverse bias (RB), voltage, temperature, both in dark and under

illumination can provide a critical guidance to design and optimize the fabrication of a solar cell [11]. However the DC characterization technique limits the identification of parameters like interfacial, diffusion and transition capacitance, and the resistive and capacitive components of p-p$^+$ interface of a silicon solar cell.

In this view, an effective approach to address this issue is now possible by employing AC characterization technique i.e. Impedance spectroscopy (IS). IS is a frequency domain technique that allows the decoupling of various physical processes associated with different interfaces of a solar cell [12–14]. Quantitative processing of IS spectra however requires an appropriate model that correlates with these physical processes. The IS technique has been amply used in various electrochemical systems such as Dye sensitized solar cell [15], organic solar cells [16], batteries [17], and solid – liquid interface [18], but there is scarcity of reports available for solid state devices like CIGS [19], CdTe [20], GaAs/Ge [21], and silicon solar cells [22]. The progress and the development of IS model for silicon based solar cell is most important due to: First, silicon solar cell stands as a reference for the entire solar production and installation industry, Second, the consistent performance, low cost and high stability in comparison with other PV technologies and Third, in the fabrication aspects, the silicon

material is homogenous without any complication of grain boundaries, multiply phases and in addition optimized electrical and optical performance [11].

In this work, the theoretical model framework for IS spectroscopy with previously reported literature and its application in the performance of silicon solar cells have been reviewed. The work is mainly focused on (i) the reviewing the development of the various impedance models for silicon solar cells (ii) elucidating the recombination and resistive losses in the fabricated solar cells, (iii) decoupling the various photovoltaic parameters associated with different physical processes in terms of resistive and capacitive elements, and (iv) analysis of relaxation time associated with the solar cells. Moreover, the experimental results along with the analytical model provide an insight into the loss mechanism and the use of a simple tool that can be integrated with the conventional photovoltaic testing.

The review article is structured as below: Section 2 discusses the different models like one diode model, two diode model and transmission line model explaining the derivation of the resistance and capacitance associated with the various junctions of a solar cell in terms of the flowchart; Section 3 briefly explains the experimental considerations to be taken care of while doing the impedance measurements; in Section 4 the importance of impedance spectroscopy to determine the various resistive and capacitive elements associated with the various interfaces of a Si solar cell is revealed through the discussion of case studies. Herein, the reports by other authors in this field is reviewed. Moreover, some important views on the application of impedance spectroscopy in the production line of Si solar cell is also presented in this section. Section 5 deals with the future aspects in the field of impedance spectroscopy and the need for the development of this technique to obtain instantaneous impedance values for nonstationary systems. This is followed by the conclusions of the review presented.

2. Theoretical considerations

Fig. 1 shows the schematic of a silicon solar cell with various regions and interfaces contributing to different capacitive and resistive components. The represented Fig. 1 also includes the elements of low-high junction and leaky Schottky barrier formed at the back contact of Al [23]. The back surface field (BSF) equipped solar cell incorporates several optical and morphological engineering elements such as random textured surface to reduce recombination, phosphorus doping for n^+ emitter formation and Aluminium doped p^+ BSF, with Ag and Al metalized contact at the front (emitter) [8].

As show in Fig. 1, the n^+-p junction located at x_j along with the depletion region width on emitter side i.e. $W_n=(N_a W_j)/(N_a+N_d)$ and on the base side i.e. $W_p=(N_d W_j)/(N_a+N_d)$ defines the total width of the space charge region (SCR) as $W_j=W_n+W_p$ [24], where N_a and N_d are acceptor and donor concentrations, respectively. The built in potential and the bias voltage across n^+-p junction are given as $V_{bi}=(K_B T/|e|)\ln(N_a+N_d/n_i^2)$ where n_i is intrinsic carrier concentration, K_B and T represents Boltzmann constant and cell temperature respectively [25]. At the interface of p-p^+ junction i.e. LH interface, holes from p^+ side diffuse into p side to form a hole accumulation layer and a depletion layer. The concentration gradient of holes at LH interface sets up a built in voltage as $(V_{p0}=(k_B T/|e|)\ln(N_a^+/N_a))$, where N_a^+ is the hole concentration in the p^+ region. The electric field induced at LH interface repels the diffuse electrons back from the n^+-p interface into the p-region. This contributes to the increase in overall cell efficiency with an increase in open circuit potential of a solar cell [26,27]. The dependence of majority and minority charge carriers at n^+-p and LH interface on voltage has been discussed by Garland et al. [8]. Thongpron et al. [28] developed a method which allows for the determination of the dynamic resistance, of the series resistance of the solar cell and of the module under both illumination and dark conditions using one diode model. Garland et al. [8] reported a generalized version of the single diode model as shown in Fig. 2. The presented Fig. 2 includes the element for LH interface and a leaky Schottky barrier formed at the Al back contact. The R_{SH} in parallel with n^+-p junction represents the shunt path for electrons and light generated net output current through R_{SH}. J'_d and J_d represents the current through LH junction and the diode current respectively.

In general, a two diode model is also employed for the analysis of a silicon solar cell. A two diode model discussed by Garland et al. [7] for quantitative evaluation of temperature and voltage dependent parameters of silicon solar cell are briefly outlined in this section. Fig. 3 shows a general two diode model to describe the DC electrical characteristics of a solar cell [7]. The AC electrical characteristics of the discussed two diode model is shown in Fig. 4[7]. In Fig. 4, R_r and R_{SH} are considered as independent resistances where R_r specifies the SCR recombination that are manifested at moderate FB. The capacitance associated with R_r is given by C_r where both these terms replace Diode 2 and denotes the resistance and capacitance of charge recombination in SCR [29,30].

Mora-Seró et al. [11] have introduced a transmission line model as an alternate approach for the modelling of silicon solar cell where circuit configurations are developed by considering the distribution of Fermi levels at selective contacts of the light absorber layer [11]. The equivalent circuits discussed for one and two diode model under
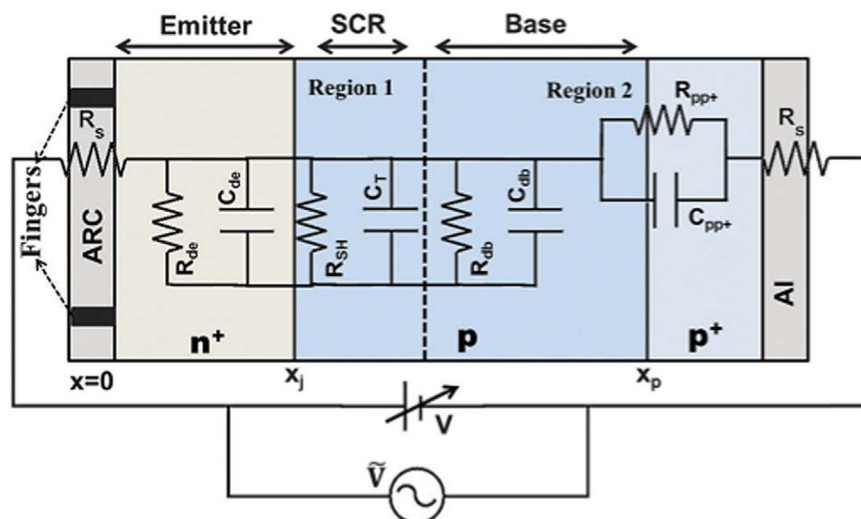

Fig. 1. Schematic of a mono-crystalline Si solar cell, with performance contributing elements from different regions [23].Reproduced from [23] with permission of The Royal Society of Chemistry.
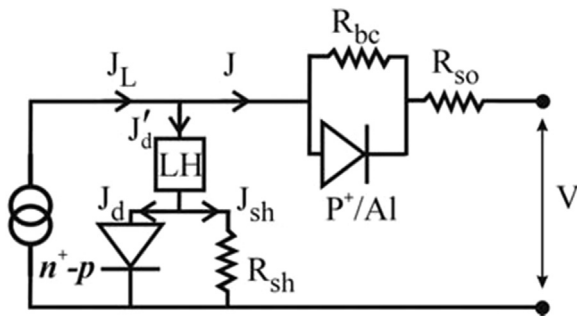
Fig. 2. The single-diode model of a crystalline silicon solar cell, with the inclusion of the L–H junction and the metal-semiconductor back contact [8].Reproduced from [8] with permission of The Royal Society of Chemistry.
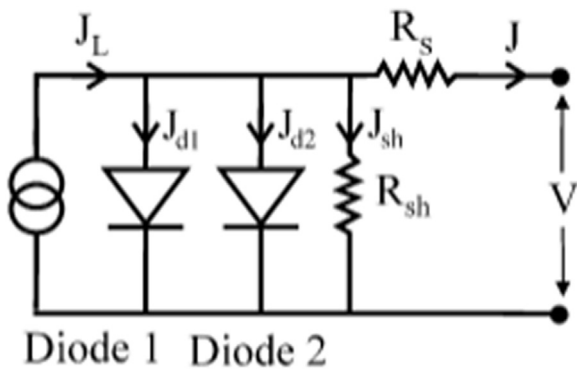

Fig. 3. A commonly used two-diode model, representing the DC response of the cell [7].Reproduced from [7] with permission of Elsevier
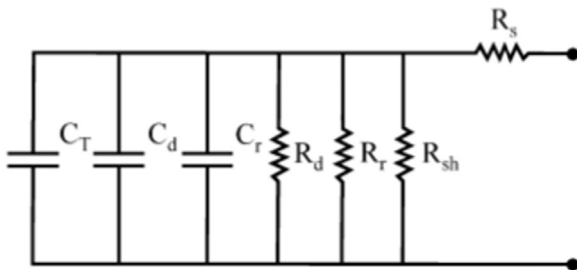

Fig. 4. AC circuit model of the solar cell, where the C_d-R_d combination replaces Diode 1.Reproduced from [7] with permission of Elsevier

certain conditions appear as transmission like network. Fig. 5 shows the transmission line model for a silicon solar cell where the model comprising of different elements relates to the electron transport resistance (r_{tr}), diffusion resistance (r_d), chemical capacitance (c_μ) and back surface recombination resistance (r_{sur}).

To derive a net impendence of the transmission line, it is assumed that the distributed circuit elements are position independent and the charge carriers are homogenously distributed in the solar cell [2]. The elements of the proposed equivalent circuit comprises of (a) a distributed transfer resistance ($r_{tr}=R_t/L$), mainly responsible for hin-

drance of electron transport (P_S), (b) a distributed chemical capacitance ($c_\mu=C_\mu/L$ represents the capacitance per unit area associated with homogenous charge accumulation (P_{sol}) and (c) recombination resistance ($r_{rec}=R_{rec}L$) accounting for the electron hole recombination.

The details of simulation of the above equation were discussed by Mora-Seró et al. [11]. The capacitive effect under illumination defines the upper limit of open circuit voltage (V_F) [31]. One diode and two diode model describes the cell operation in terms of V_j, and then, with the introduction of the transmission line model, the description quickly switches over to V_F. These two notations are frequently used in the literature for describing the cell operation. Here, V_j describes the n$^+$p junction potential under forward bias condition where the contributions from the series resistance is subtracted. However, V_F defines the potential due to the splitting of Fermi level which arises from the accumulation of minority carriers. The potential difference between electron and hole Fermi-level defines the maximum achievable open circuit voltage (V_F) in a solar cell [32]. Different models like one diode model (Scheme 1), two diode model (Scheme 2) and transmission line model (Scheme 3) explaining the derivation of the resistance and capacitance associated with the various junctions of a solar cell is shown in terms of flowchart.

3. Experimental considerations specific to impedance spectroscopy of solar cells

The instrument does not always auto-select the proper current range for the IS measurement and hence the current range must be set to obtain adequate IS data without instrumental artifacts. Garland et al. [8] have shown the influence of current range setting on the measured IS data. The IS data collected with auto-range setting appeared noise-free, but a simple examination of only the overall curve can be deceptive. As in the linear sweep voltammetry, where the low and high currents have to be inspected, in IS, the low and high frequencies have to be inspected. The fixed and auto-range data should have the same low frequency intercept. Only the presence of such a coincidence of intercepts confirms that the system temperature has remained constant throughout both the collection runs. This generally must be the case, unless experimental artefacts interfered, as the temperature of the cell is externally controlled. It was shown by Garland et al. and co-workers [29] that the low frequency (LF) data gets distorted on the 200 mA range and the high frequency (HF) data is distorted on auto-range. The same ranges of frequencies were collected for both runs, but the auto-range data are shifted significantly downward by inductive reactance. This is because the 200 mA range has a significantly smaller system inductance than the 2 mA range selected by the potentiostat.

The values of the DC bias voltage and current are recorded at the beginning of the collection of IS data. At the end of the IS data collection, if the spectrum has reached low enough in frequency, this initial resistance, should agree with the observed LF intercept; if not the temperature may have changed during the data collection. These considerations are incorporated in the checks for possible cell temperature variations during IS measurements. Usually a perturbation voltage setting of 5 mV-rms allows the system to operate adequately below $K_BT/|e|$ and avoids nonlinear effects in IS. However, nonlinear (non-ohmic) DC effects can also interfere with AC IS measurements.
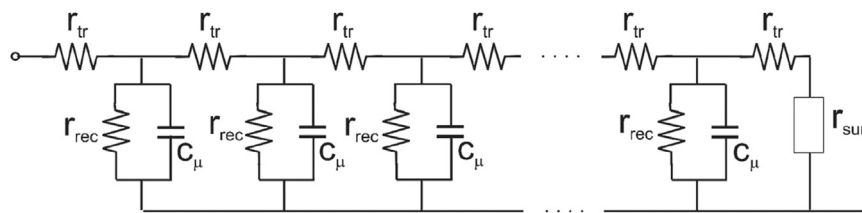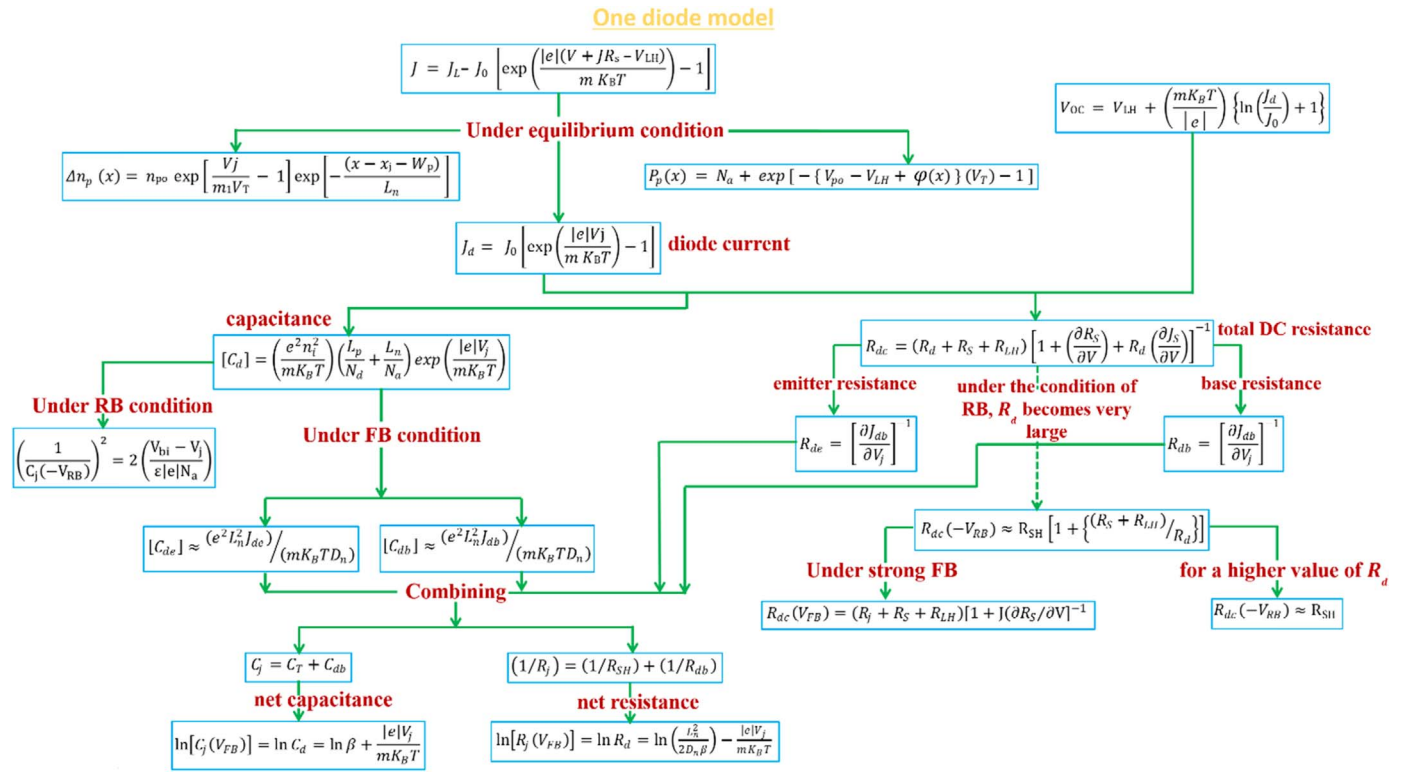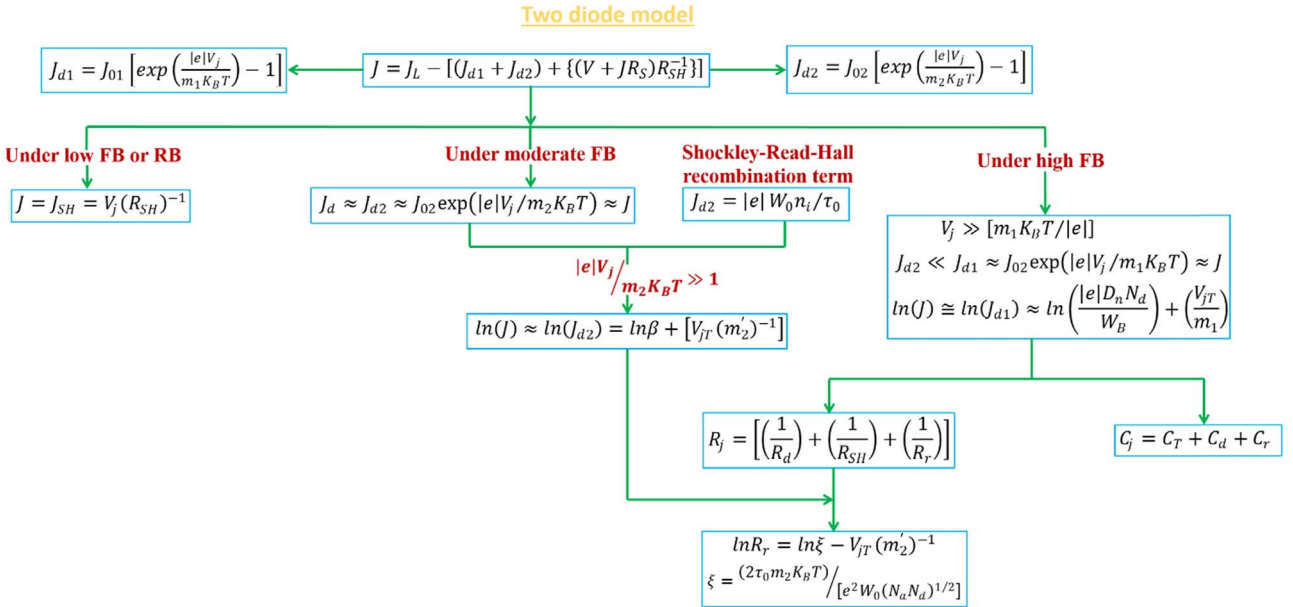

Fig. 5. The transmission line representation of the diffusion–recombination impedance with the surface recombination resistance r_{sur}, that gives an ohmic contact boundary condition for $r_s\rightarrow0$[11].Reproduced from [11] with permission of The Royal Society of Chemistry

One diode model

$$J = J_L - J_0 \left[\exp\left(\frac{|e|(V + JR_s - V_{LH})}{m K_B T}\right) - 1\right]$$

Under equilibrium condition

$$V_{OC} = V_{LH} + \left(\frac{mK_BT}{|e|}\right)\left\{\ln\left(\frac{J_d}{J_0}\right) + 1\right\}$$

$$\Delta n_p(x) = n_{po}\exp\left[\frac{Vj}{m_1 V_T} - 1\right]\exp\left[-\frac{(x - x_j - W_p)}{L_n}\right]$$

$$P_p(x) = N_a + \exp\left[-\{V_{po} - V_{LH} + \varphi(x)\}(V_T) - 1\right]$$

$$J_d = J_0\left[\exp\left(\frac{|e|Vj}{m K_B T}\right) - 1\right] \quad \textbf{diode current}$$

capacitance

$$[C_d] = \left(\frac{e^2 n_i^2}{mK_BT}\right)\left(\frac{L_p}{N_d} + \frac{L_n}{N_a}\right)\exp\left(\frac{|e|V_j}{mK_BT}\right)$$

$$R_{dc} = (R_d + R_S + R_{LH})\left[1 + \left(\frac{\partial R_S}{\partial V}\right) + R_d\left(\frac{\partial J_S}{\partial V}\right)\right]^{-1} \quad \textbf{total DC resistance}$$

emitter resistance   **under the condition of RB, R_d becomes very large**   **base resistance**

Under RB condition

$$\left(\frac{1}{C_j(-V_{RB})}\right)^2 = 2\left(\frac{V_{bi} - V_j}{\varepsilon|e|N_a}\right)$$

Under FB condition

$$R_{de} = \left[\frac{\partial J_{db}}{\partial V_j}\right]^1$$

$$R_{db} = \left[\frac{\partial J_{db}}{\partial V_j}\right]^1$$

$$R_{dc}(-V_{RB}) \approx R_{SH}\left[1 + \left\{(R_S + R_{LH})/R_d\right\}\right]$$

$$[C_{de}] \approx \frac{(e^2 l_n^2 J_{de})}{(mK_BTD_n)}$$

$$[C_{db}] \approx \frac{(e^2 l_n^2 J_{db})}{(mK_BTD_n)}$$

Combining

Under strong FB   **for a higher value of R_d**

$$R_{dc}(V_{FB}) = (R_j + R_S + R_{LH})[1 + J(\partial R_S/\partial V]^{-1}$$

$$R_{dc}(-V_{RH}) \approx R_{SH}$$

$$C_j = C_T + C_{db}$$

$$(1/R_j) = (1/R_{SH}) + (1/R_{db})$$

net capacitance   **net resistance**

$$\ln[C_j(V_{FB})] = \ln C_d = \ln\beta + \frac{|e|V_j}{mK_BT}$$

$$\ln[R_j(V_{FB})] = \ln R_d = \ln\left(\frac{l_n^2}{2D_n\beta}\right) - \frac{|e|V_j}{mK_BT}$$

Scheme 1. The flow chart showing the derivation of resistance and capacitance from the J-V equations using one diode model. All the notations used in equations are defined in Appendix A.
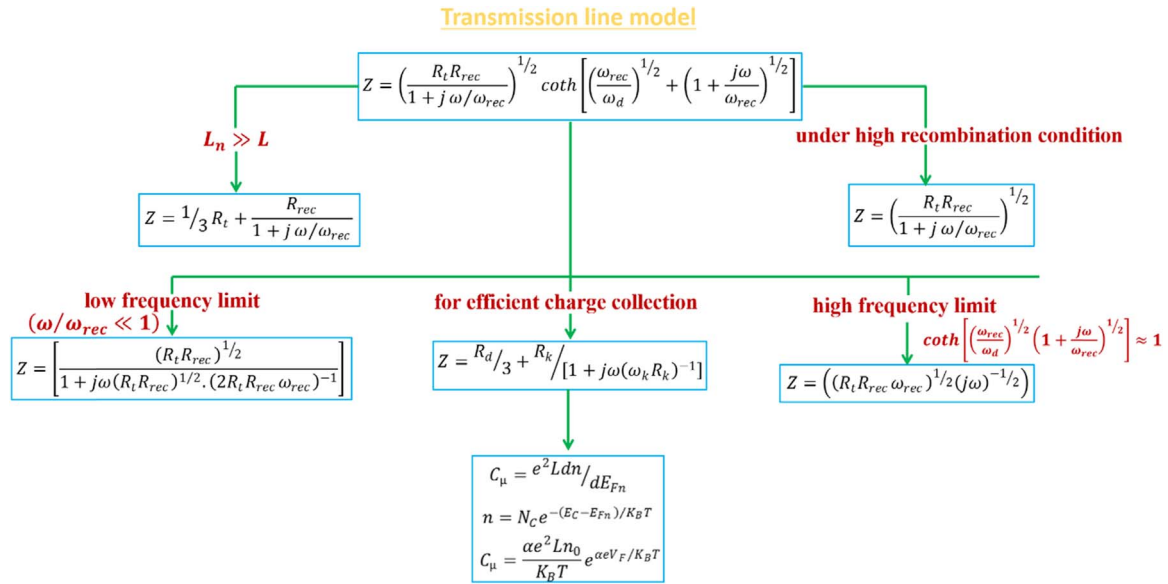
Two diode model

$$J_{d1} = J_{01}\left[\exp\left(\frac{|e|V_j}{m_1 K_B T}\right) - 1\right]$$

$$J = J_L - [(J_{d1} + J_{d2}) + \{(V + JR_S)R_{SH}^{-1}\}]$$

$$J_{d2} = J_{02}\left[\exp\left(\frac{|e|V_j}{m_2 K_B T}\right) - 1\right]$$

Under low FB or RB   **Under moderate FB**   **Shockley-Read-Hall recombination term**   **Under high FB**

$$J = J_{SH} = V_j(R_{SH})^{-1}$$

$$J_d \approx J_{d2} \approx J_{02}\exp(|e|V_j/m_2 K_B T) \approx J$$

$$J_{d2} = |e|W_0 n_i/\tau_0$$

$$V_j \gg [m_1 K_B T/|e|]$$

$$J_{d2} \ll J_{d1} \approx J_{02}\exp(|e|V_j/m_1 K_B T) \approx J$$

$$\ln(J) \cong \ln(J_{d1}) \approx \ln\left(\frac{|e|D_n N_d}{W_B}\right) + \left(\frac{V_{jT}}{m_1}\right)$$

$$|e|V_j/m_2 K_B T \gg 1$$

$$\ln(J) \approx \ln(J_{d2}) = \ln\beta + [V_{jT}(m_2')^{-1}]$$

$$R_j = \left[\left(\frac{1}{R_d}\right) + \left(\frac{1}{R_{SH}}\right) + \left(\frac{1}{R_r}\right)\right]$$

$$C_j = C_T + C_d + C_r$$

$$\ln R_r = \ln\xi - V_{jT}(m_2')^{-1}$$
$$\xi = \frac{(2\tau_0 m_2 K_B T)}{[e^2 W_0 (N_a N_d)^{1/2}]}$$

Scheme 2. The flow chart showing the derivation of resistance and capacitance from the J-V equations using two diode model. All the notations used in equations are defined in Appendix A.

Sometimes these latter effects can be more dominant than those introduced by a perturbation voltage that is larger than 5 mVrms. This point is well illustrated by Garland et al. and co-workers [8–10].

The first and simplest choice about the frequencies in the spectrum is how many to collect. Each frequency is a separate measurement and improves the statistical uncertainty. Certain considerations also apply to the selection of the frequency range of AC perturbation for IS. If possible, it is preferred that the recorded Nyquist spectrum intercepts the Z' axis at both the low and the high frequency ends of the spectrum. However, to avoid over-clustering of data points in a limited frequency space, excessive points at the low or high frequency end are not collected. Collecting more frequencies below this intercept would result in too many samples gathering up on the real axis. This would cause the frequency weighting to favor fitting this region of the spectrum over the quality of the fit in the HF region of the spectrum. It is reasonable to go below the real axis at the HF region of the curve because the steeper the slope becomes the more the change in Z is due to just a change in reactance. In other words the value of Z' stops changing with frequency and acquires the value of the series resistance. More points like that in the spectrum lower the uncertainty in the series resistance and system

Transmission line model

$$Z = \left(\frac{R_t R_{rec}}{1 + j\omega/\omega_{rec}}\right)^{1/2} coth\left[\left(\frac{\omega_{rec}}{\omega_d}\right)^{1/2} + \left(1 + \frac{j\omega}{\omega_{rec}}\right)^{1/2}\right]$$

$L_n \gg L$

$$Z = \frac{1}{3}R_t + \frac{R_{rec}}{1 + j\omega/\omega_{rec}}$$

under high recombination condition

$$Z = \left(\frac{R_t R_{rec}}{1 + j\omega/\omega_{rec}}\right)^{1/2}$$

low frequency limit
$(\omega/\omega_{rec} \ll 1)$

$$Z = \left[\frac{(R_t R_{rec})^{1/2}}{1 + j\omega(R_t R_{rec})^{1/2} \cdot (2R_t R_{rec}\omega_{rec})^{-1}}\right]$$

for efficient charge collection

$$Z = \frac{R_d}{3} + \frac{R_k}{[1 + j\omega(\omega_k R_k)^{-1}]}$$

high frequency limit

$$coth\left[\left(\frac{\omega_{rec}}{\omega_d}\right)^{1/2}\left(1 + \frac{j\omega}{\omega_{rec}}\right)^{1/2}\right] \approx 1$$

$$Z = \left((R_t R_{rec} \omega_{rec})^{1/2}(j\omega)^{-1/2}\right)$$

$$C_\mu = e^2 L \frac{dn}{dE_{Fn}}$$

$$n = N_c e^{-(E_C - E_{Fn})/K_B T}$$

$$C_\mu = \frac{\alpha e^2 L n_0}{K_B T} e^{\alpha e V_F / K_B T}$$

Scheme 3. The flow chart showing the derivation of resistance and capacitance using transmission line model. All the notations used in equations are defined in Appendix A.

inductance. Moreover, the potentiostat allows a logarithmic or linear spacing of frequencies in the AC perturbation spectrum used for IS. Garland et al. [29] have shown that a linear spacing does not properly weight the LF region of the spectrum while a logarithmic spacing does not properly weight the HF region of the spectrum.

4. Discussion of case studies

Garland et al. [8] reported IS spectra obtained at 25 °C for silicon solar cells with controlled variation of DC bias. Fig. 6 represents the complex Nyquist spectra as a function of applied bias where the line and symbols represent the theoretical and experimental data, respectively. The complex spectra at reverse bias and weak forward bias follow the description of single time constant. As the bias across the n+-p junction increases, the radii of semi-circular Nyquist spectra decreases due to an increase in the conductivity of the diode. With the further increase in the DC bias, the Nyquist spectra displays a two time constant where the solar cell behaves like a n+-p diode at relatively low frequency and p-p+ BSF at a higher frequency.

The transition between single time constant to two time constants signifies the dependence of IS on the applied DC bias. In the low FB, the contribution from p-p+ junction is not detected in the IS spectra until a strong FB greater than knee voltage of the diode is applied. This is mainly because at moderate FB, the bias across n+-p and p-p+ junction compresses the space charge layer and the junction width. Also, the p-p+ junction is comparatively thinner than the n+-p diode and the base of a solar cell. Hence, the net impedance at low FB is mainly dominated by the much larger impedance offered by the n+-p diode. Therefore, in order to obtain a satisfactory fit of the experimental data, a two series time constant needs to be considered [2,3].

Sanjai et al. [33] has used IS on p+-p-n structure under both FB and RB condition to obtain generation and recombination lifetime, respectively. The p+-p and p−n junction was formed on both the sides of a silicon wafer by thermal evaporation of semi-transparent metal layers of palladium and aluminium, respectively. During the sample preparation no thermal treatment was given to the device so that diffusion of impurities cannot penetrate inside the semiconductor and junction. Sanjai et al. [33] also found a similar bias dependence of the p+-p and p−n junction under forward and reverse bias as discussed by Garland et al. [8,9]. However based upon the obtained spectra, Sanjai et al. [33,34] extended their analysis by finding and comparing the generation and recombination lifetime of silicon wafer with conventional

micro wave detected Photoconductive decay (μ-PCD) measurements. The recombination lifetime of silicon wafer were calculated from the obtained Nyquist spectra at FB. It has been shown by Sanjai et al. [33] that an increase in the FB can lower the lifetime of charge carriers and this can be easily understood in terms of the surface recombination velocity (s). Based upon the obtained recombination lifetime from Nyquist spectra and bulk lifetime of the silicon wafer, the surface recombination velocity can be easily found by using the expression [35] $1/\tau_{rec} = 1/\tau_{bulk} + S/d$, where, d is the wafer thickness. The authors have concluded that the generation and recombination are measured under the RB and FB condition respectively. The generation lifetime was estimated to be around 73 μs whereas the recombination lifetime was found to be about 11 μs. The minority carrier lifetime as measured by μ-PCD method on the same sample was 12 μs which was much closer to the measured recombination values by IS. This signifies that IS can be used to measure the effective lifetime of wafer using an induced junction structure prior to the fabrication of an actual device. Recently, Thouti et al. [36] estimated passive components of cells like; series resistance, recombination resistance, and chemical capacitance using impedance spectroscopy which were further used for estimating effective carrier lifetime (τ_{eff}) values. The Ag NPs on cells without Si3N4 spacer layer exhibited a small decrease in τ_{eff} due to surface field effect passivation by NPs. The Ag NPs on the cell with Si3N4 spacer layer exhibited a large decrease in seff due to the parasitic absorption losses. The parasitic absorption losses from Ag NPs influenced the passive components by suppressing light transmission into the plasmonic cell, which led to a decrease in τ_{eff}.

Mora-Seró et al. [11] measured a set of IS spectra for different illumination intensities in both FB and RB conditions for a small BP silicon solar cell. Fig. 7 depicts the IS for three different Illumination intensities. The obtained IS spectra basically shows a semicircle that can be described by a simple circuit consisting of a series resistance (R_S) in series with parallel combination of $R_P - C$. At high FB condition, an inductive behaviour is observed in the high frequency range. For a silicon solar cell, inductance has no meaning but the use of inductive element in the equivalent circuit improves the determination of physical parameters. Additionally, at a higher FB a distorted semicircle is observed at high frequency, which is consistent with the results of other authors [37]. Mora-Seró et al. and his co-authors explained that this is due to the chemical capacitance of holes [38] and the associated resistance is much smaller in magnitude as compared to the resistance associated with electron chemical capacitance. In the case of small solar
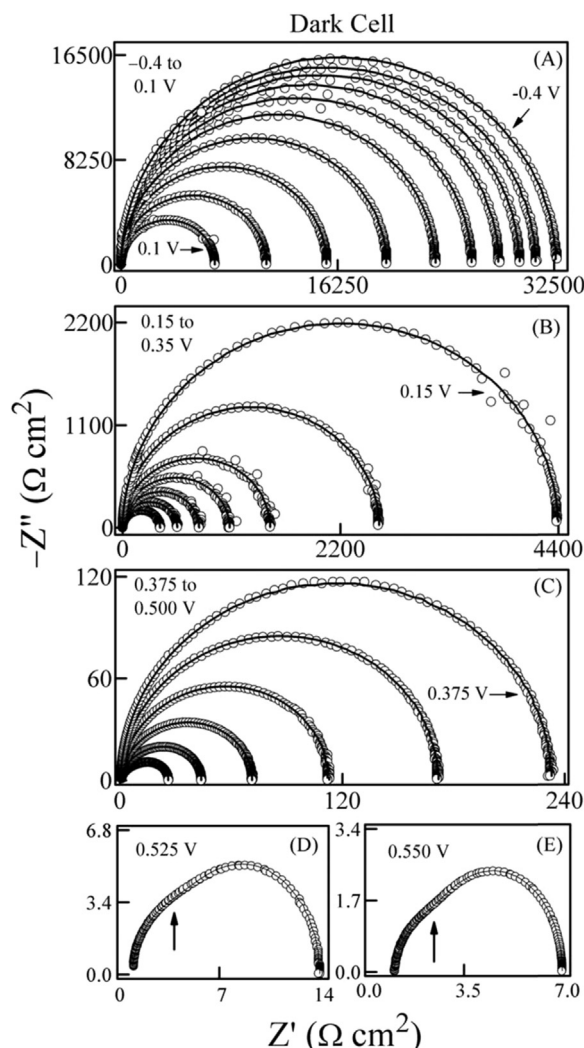
Fig. 6. Nyquist spectra for a dark cell recorded at various DC voltages. The symbols represent experimental data and the lines are CNLS fits to the data using the circuit model of Fig. 2C. In (A), the plots of successively decreasing radii were collected at gradually increasing DC voltages in the following order: V=−0.400, −0.300, −0.250, −0.200, −0.150, −0.100, −0.500, 0, 0.050 and 0.10 V. In (B), the plots of large to small radii correspond to V=0.150, 0.200, 0.250, 0.275, 0.300, 0.325, and 0.350 V. The plots of successively decreasing radii in (C) were recorded at 0.375, 0.400, 0.425, 0.450, 0.475, and 0.500 V. In (D) and (E), the diode of the solar cell was forward biased at V=0.525 and 0.550 V, respectively, where the spectral signatures of the C_{LH}−R_{LH} loop appeared and became more prominent with increasing voltages. The vertical arrows in (D) and (E) indicate the approximate frequency region indicating the transition between the two time constants ($R_{LH}C_{LH}$) and (R_jC_j). [8].Reproduced from [8] with permission of The Royal Society of Chemistry.

cell samples the inspection of experimental IS in high frequency region does not reveal a Warburg behaviour. The Warburg behaviour could have been disguised by the inductance or the hole capacitance. The DC resistance obtained from IS measurement at different illumination intensities are given as $R_{dc}=R_S+R_P$. Mora-Seró et al. [11] has shown that by using the IS measurements it is possible to discriminate between the two contributions given in the above equation. The authors have measured R_S using two different experimental conditions: (a) at dark, by applying a DC bias with the Fermi level fixed by the applied potential and (b) under different illumination, by applying a bias voltage equal to V_{OC}. A similar behaviour for R_S has been found by normalizing the value of R_S with respect to cell area. This signifies that R_S depends on the Fermi level position and it does not only describes the resistance due to connection leads.

Sanjai et al. [39] studied the silicon solar cell at different illumina-

tion intensities and wavelengths using IS. To obtain a satisfactory fit of the experiment data, they employed the same equivalent circuit as discussed for the p-i-n solar cell under illumination [40]. The equivalent circuit for the solar cell is derived from a static equivalent circuit by replacing the diode with the junction transition capacitance and diffusion capacitances, and its dynamic resistances. The solar cell structure with its equivalent AC circuit is shown in Fig. 8, wherein a single RC circuit consists of a parallel resistor (R_P) and capacitor (C_P), and R_S is the series resistance of the device. Authors have presumed that under illumination the entire light sensitive component in the structure provides a virtual RC network parallel to the initial R_PC_P.

Fig. 9 shows the IS Spectra in dark and under heterogeneous light at different illumination intensities. It was found that with the change in illumination the values of R_S,R and C were changed. As compared to the dark condition, the value of R_S under illumination is comparatively higher. They have also calculated the value of R_S using Avaujo's area method [41]. The value of R_S calculated from the illuminated J-V curve at AM 1.5 was found to be close to the value determined from IS under illumination. However, the extracted value of R and C showed an opposite trend where the value of R decreases and C increases with the illumination. The phenomena of increase in the value of C can be explained by M bore's model [42,43]. Under the open circuit condition, the value of capacitance does not change whereas under the short circuit condition an extra capacitance is added and an effective capacitance is defined as [43] $C_{eff}=C_d[1 + \delta]$. Here, δ is proportional to the excess carrier concentration (Δn) which directly depends upon P_{in}. Sanjai et al. [33] has coupled the analysis of IS with spectral response of the solar cell and concluded that the IS spectra starts shrinking from low λ (400 nm) up to 850 nm from where it starts expanding. These results were further supported by spectral response (SR) and quantum efficiency (QE) data where minimum value of R_I was corresponding to the maximum value of SR at 850 nm i.e. both the trends were complementary to each other.

A combined effect of V_j and T on the IS parameters of a silicon solar cell were studied by Garland et al. [7]. Fig. 10A shows experimental Nyquist spectra of a silicon solar cell recorded for different cell temperature at 0V and the Nyquist spectra for different junction voltage is shown in Fig. 10B. The plot in Fig. 10A is acquired under the dark condition at V_{OC} to avoid any temperature induced fluctuations due to the voltage drop by JR_S. The obtained combined spectra (V_j & T) suggest that the shunt resistance R_{SH} is largely voltage independent while C_T depends upon the variation of both V_j and T.

The results obtained by Garland et al. [7] describe an experimental strategy for coupling IS with linear scan voltammetry to explore the various temperature and bias dependent parameters of a silicon solar cell. The IS spectra recorded as a function of temperature resolves the temperature dependent behaviour or trend of the SCR capacitance, resistance, shunt and SCR recombination. The values of R_S and V_{bi} measured by IS are used for adequate normalization of DC bias where the different thermal components of the junction voltages are combined in a single scaled parameter. The studies by Garland et al. [7] elucidate the complex mechanisms associated with the temperature and voltage sensitive characteristics of a silicon solar cell using the available theoretical model.

More recently, Cotfas et al. [44] reviewed the behaviour of various thin film, dye sensitized solar cells, organic and multi-junction solar cells in dynamic regime using impedance spectroscopy technique. The author presents the methods which allow the determination of either of all ac parameters of solar cells or only one of them. The methods analyzed allow measuring the dynamic impedances using the frequency and time domain techniques. It also discusses the methodologies to determine the dc parameters of solar cells from the variation of the capacitance applying reverse and forward bias. The different types of the solar cells ac equivalent circuits from a proper fitting are also discussed in the paper.
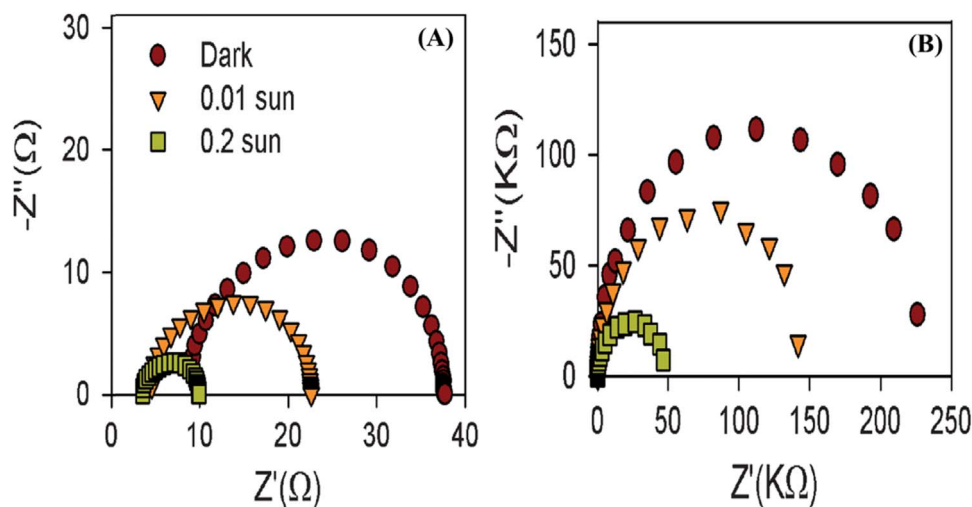
Fig. 7. Impedance spectra for three different illumination intensities (A) Forward bias V=−0.2 V (B) Reverse bias V=0.5 V (small BP solar cell) [11].Reproduced from [11] with permission of The Royal Society of Chemistry.
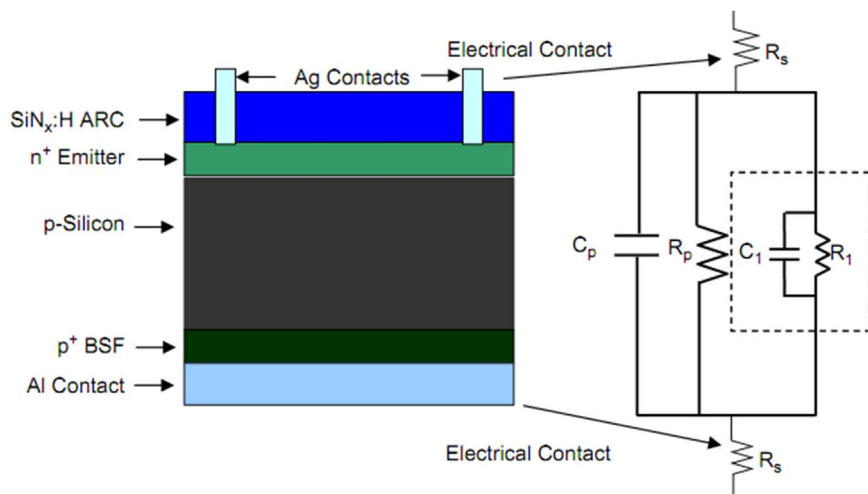

Fig. 8. Solar cell structure and its equivalent electrical circuit [33].Reproduced from [33] with permission of Elsevier.
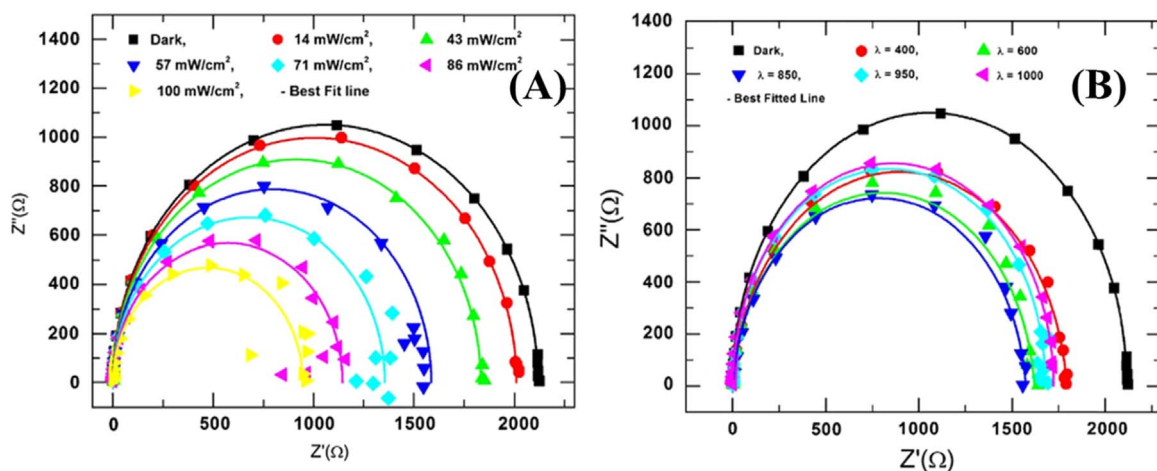

Fig. 9. (A) Complex impedance spectra in dark and under different intensities (14, 43, 57, 71, 86, 100 mW/cm²) of illumination, (B) Complex impedance spectra in dark and at different (400, 600, 850, 1000 nm) wavelength of irradiation. The symbols represent experimental points and the lines gives best fit curves from Z-plot software [33].Reproduced from [33] with permission of Elsevier.

4.1. Resistive and capacitive components of n⁺-p junction

The behaviour of the resistive and capacitive parameters of n⁺-p junction with respect to the change in junction bias, illumination and

temperature can provide a critical guidance to design and optimize the fabrication of a solar cell. Fig. 11 shows the trend of R_S and n⁺-p junction resistance (R_j) measured at 25 °C at different levels of sun illumination (0–1 sun) as a function of V. It has been seen in Fig. 11A
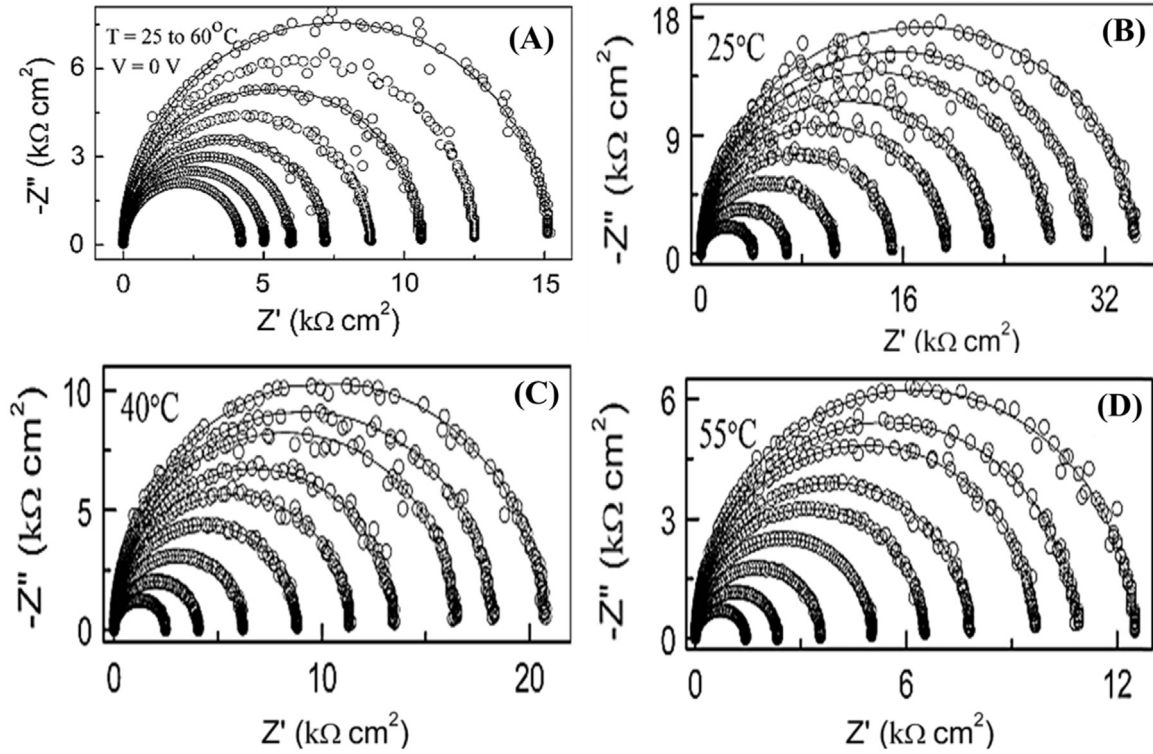
Fig. 10. (A) Nyquist spectra recorded at 0.0 V (V_{OC}) for a dark Si solar cell at different temperatures. The plots of successively decreasing radii correspond to increasing cell temperatures in the order, 25, 30, 35, 40, 45, 50, 55, and 60 °C, Nyquist spectra for a dark Si solar cell, collected at different DC bias voltages, with the cell temperature maintained at (B) 25, (C) 40 and (D) 55 °C [7]. Reproduced from [7] with permission of Elsevier.
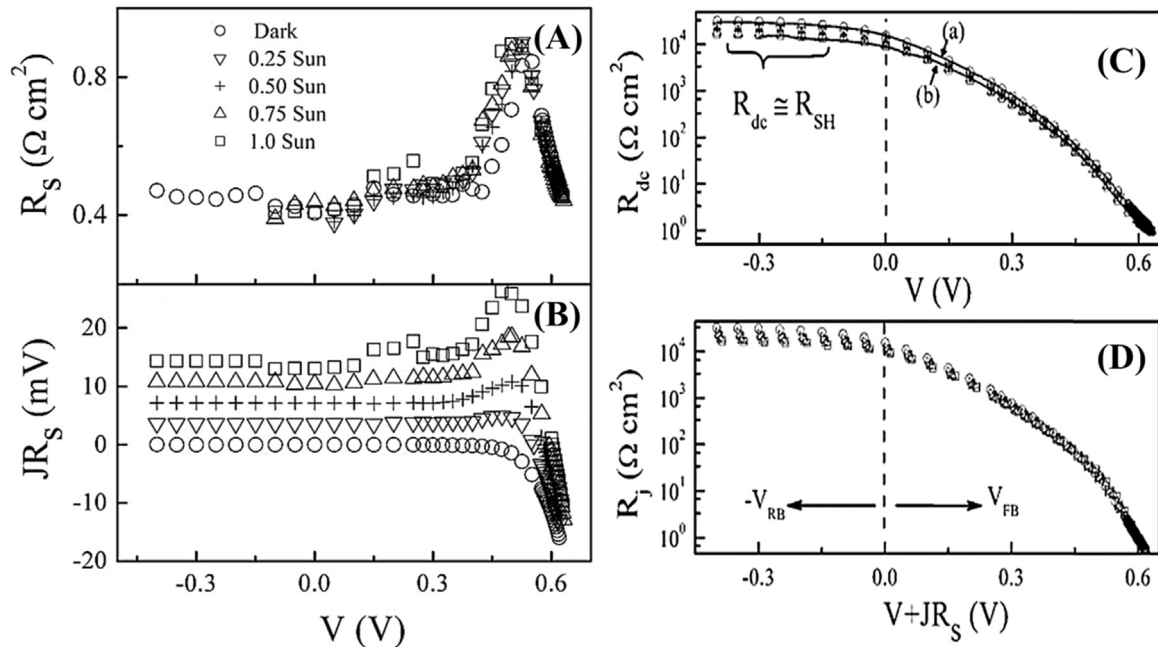
Fig. 11. (A) Surface area-normalized series resistance R_S, (B) voltage drop at R_S for a temperature (25 °C) controlled Si solar cell, as functions of illumination and terminal voltage of the cell, (C) lines (a) and (b) represent R_{dc} as the inverse slope of the J–V plots recorded at 0 and 1 sun illuminations, respectively and (D) resistance of the n⁺–p diode junction, measured using IS at different illuminations [8]. Reproduced from [8] with permission of The Royal Society of Chemistry.

that the voltage axis has not been scaled to V_j and the obtained values of R_S under different illumination follows the same trend by overlaying each other [8]. The voltage dependent plot of R_S showed a mixed behaviour of ohmic and non-ohmic components. In the low FB region, a dominance of ohmic component is there due to the Schottky diode. This diode does not act itself as a source of photocurrent at ≤ 1 sun illumination [45,46]. A non ohmic term of R_S in the bias range close to

knee voltage of a solar cell is associated with Al/p⁺-Si contact, where Al forms a low barrier Schottky diode [47]. Schroder et al. [48] have shown that the tunnelling current through such diode varies as a function of voltage drop across the diode. The other authors [49] have also referred this tunnelling resistance to display a potential induced maximum at the Fermi degeneracy of the semiconductor.

The results of DC and AC measurements for silicon solar cells were

examined by observing the trend of R_{dc} calculated from J-V and IS measurement. Fig. 11C & D examines the trend of $R_{dc}(V)$ and $R_j(V_j)$ respectively. The symbols represent the term $(R_j+R_S+R_{LH})$ where individual resistance values were calculated from IS spectra. The line through the symbols denotes the value of R_{dc} obtained from the J-V plot. The mutual agreement between IS and J-V results confirms the validity of the measurement. In the RB and low FB region, the values of R_{dc} are mainly dominated by R_j whereas at a strong FB, $R_j \approx R_d$ and R_{dc} becomes considerably larger than $R_j(R_d)$ [8]. A linear fit to the composite IS data shown in Fig. 11D, results in the value of ideality factor 'm'. The variation in the junction capacitance C_j was also studied by the authors [8]. It was shown that under strong FB, the value of C_j is mainly dominated by C_d with an exponential dependence on V_j. By taking a linear fit to the plot of $C_d(V_j)$, the value of 'm' can be determined. The author has reported that the value of m obtained from $C_d(V_j)$ is 17% lower than the value obtained from $R_d(V_j)$ plots. This may be due to the faster rate of change in C_d than that of R_d. Also C_d acts as a DC blocking element that only depends on the width and the density of diffusion region, wherein R_d is the DC diode through which the current flows. Therefore in comparison to C_d, current carrying element R_d might be more sensitive to the presence of defects and recombination [49].

The variations in the values of n$^+$-p junction capacitance, resistance and minority carrier lifetime as a function of applied bias and illumination level were discussed by Mora-Seró et al. Fig. 12 [11] depicts the plot of C as a function of junction voltage for different light intensities. A constant value of minority carrier lifetime (10 µs) was obtained for the tested samples. The authors predicted that as compared to their small solar cells, for a complete solar cell with edge passivation a higher value of lifetime $\approx$20 µs is expected. The value of lifetime below the knee voltage has no physical meaning because in this region the cell capacitance and resistance are governed by the depletion capacitance and shunt resistance whereas beyond the knee voltage a constant value of lifetime is obtained because C_μ scales linearly with cell area and R_P scales linearly with the inverse of area. The authors have also calculated the change in the charge carrier density with change in the illumination level. When the solar cell is under illumination condition, it is assumed that additional charge carriers of each kind are equal in number i.e. $\Delta n = \Delta p$. The additional majority carriers are assumed to be removed from the depletion region by leaving the ionized impurities with the additional minority carriers generated due to the illumination. The values of $N_A + \Delta n$ were calculated by considering $N_A + \Delta n \ll N_D + \Delta p$ for different light intensities. They have found that depletion region only improves by 20% for 1 sun illumination condition

and as a consequence the carrier density n in the bulk is mainly controlled by the applied bias rather than the illumination. Fig. 12A supports or explains the similar behaviour of C_μ for different illumination intensity.

In our previous work [2], the influence of the light concentration on charge carrier recombination process and quasi Fermi levels have been explored by applying a forward bias $V_{fb} \cong V_{OC}$ across the junction. The IS measurement were carried out on the polycrystalline silicon solar cell and plotted as a Cole-Cole or Nyquist plot. Fig. 13A shows the behaviour of capacitance extracted from low frequency arc of IS spectra as a function of applied bias and light intensity.

At moderate and high FB, diffusion capacitance increases exponentially because of the occupation of electronic density of states (DOS) by the excess minority charge carriers. The observed variation of diffusion capacitance with the applied bias indicates the electronic state distribution in the band gap [2]. With an increase in the illumination level, the introduction of excess extra holes leads to an insignificant change in the majority carriers and Fermi level. As compared to majority charge carriers, the minority electron carrier density in equilibrium is negligible and the electron Fermi level changes significantly when carriers are generated under the illumination condition. Along with the junction capacitance another factor that influences the solar cell performance is the recombination process. The electron-hole pair generated under illumination can recombine before arriving to the contacts by eventually reducing the maximum achievable efficiency of a solar cell. Fig. 13B shows the variation of junction resistance extracted from the low frequency arc of IS spectra as a function of illumination and junction bias. The junction resistance follows the same trend as previously discussed by other authors [7,8,11]. The results shown here along with J-V characteristics confirm that the commercially available polycrystalline silicon solar cell can work satisfactorily under low concentration (< 3.5 suns), whereas at high concentration the dominance of QNR over SCR can lead to decrease in the η of a solar cell.

The temperature and voltage dependent variation of n$^+$-p junction capacitance and resistance were examined by Crain et al. [9] and is shown in Fig. 14. The plot of capacitance shows a change in slope from low FB to high FB because of the change in predominant recombination process from SCR to QNR. These two recombination processes are defined by the associated diode ideality factor m_2 and m_1. It has been reported that the slope of these graphs (Fig. 14) are inversely proportional to the respective diode ideality factor wherein at low FB m_2 dominates and in high FB m_1 dominates. These slopes are also inversely proportional to T (through V_T) and their voltage dependent variation in response to the different values of m_1 and m_2 are most
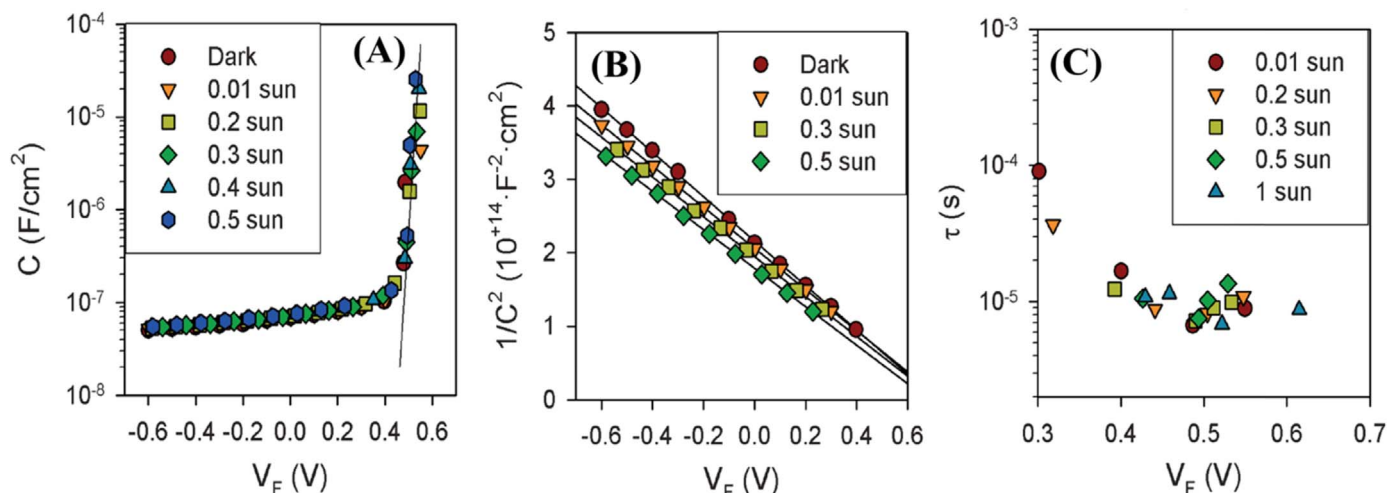

Fig. 12. (A) Device capacitance as a function of V_F, for different light intensities, (B) Mott–Schottky C^{-2} vs. V_F plot, considering only the values of capacitance where C_{dl} is the main contribution to the cell capacitance (small BP solar cell) and (C) minority carrier lifetime as a function of Fermi level potential. [11].Reproduced from [11] with permission of The Royal Society of Chemistry.
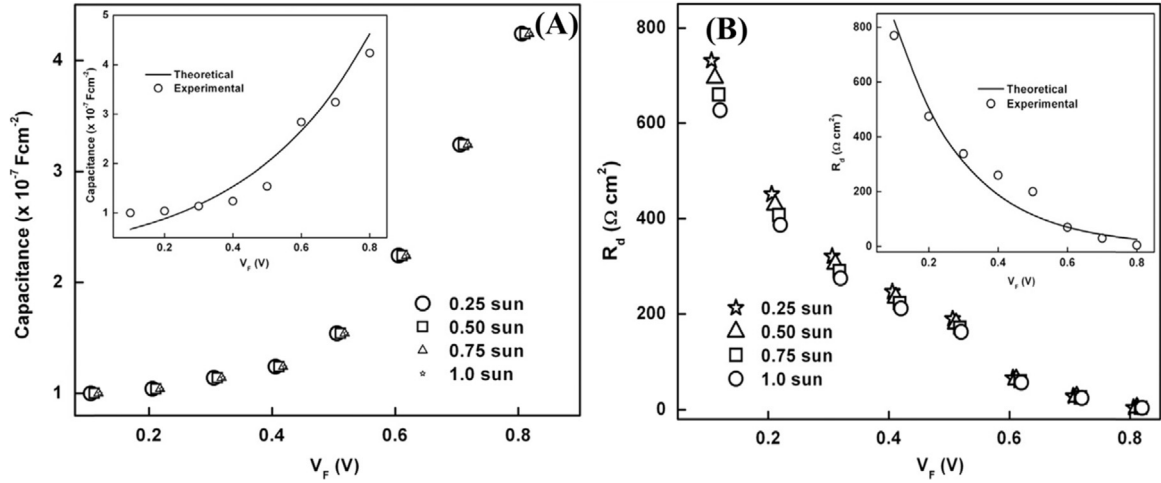
Fig. 13. (A) Variation of C_{μ} as a function of voltage for various light intensities and (B) diffusion resistance (R_d) as a function of applied bias for various light intensities. [2].Reproduced from [2] with permission of Elsevier

noticeable [9]. However as shown in Fig. 14 only the bias range above knee voltage is selected where the contribution from R_{SH} and C_T is negligible. Therefore under the experimental condition, the junction resistance and capacitance are given by $R_j=(R_{d1}R_{d2})/(R_{d1}+R_{d2})$ and $C_j=C_{d1}+C_{d2}$. The impedance element ($R_{d1}-C_{d1}$) defines the charge recombination mechanism due to the diffusion of charge carriers in the QNR of the solar cell.

The above condition is only valid to a situation where the contribution from SCR recombination is low. The capacitance C_{d1} is given as $C_{d1}=(dQ/dy)$ where Q is the total charge of diffused minority carriers. The analytical expression of C_{d1} is given as, $C_{d1}=C_{d1}^0 exp(\frac{Vj}{m1VT})=\frac{\tau1}{\alpha R_{d1}}$, where, $C_{d1}^0=(|e|lnn_{p0})/(m1VT)$ and $\tau1$ is the lifetime of minority carrier electron. Here $\tau1=2R_{d1}C_{d1}$, and a factor of 2 is included because the value of C_{d1} measured with IS in the static limit is half of the actual DC value of this capacitance. Under moderate FB the net resistance of n$^+$-p diode has the form of [50], $R_j=[2C_{d1}(\tau_1)^{-1}+2C_{d2}(\tau_2)^{-1}]^{-1}$. As per this and the shown plot of R_j and C_j in Fig. 14, it is observed that at a given temperature R_j contains the inverse voltage dependencies of C_j, where the nearly linear semi-log plots of R_j have opposite slopes of C_j. A close examination of the capacitance and resistance plot (Fig. 14) indicates that the linear slopes obtained from a given voltage region of the R_j data at specific temperature is somewhat different from the inverse of their corresponding counterparts in the capacitance data. The influence of the temperature and voltage on the effective carrier lifetime of silicon solar cell was also analyzed by these authors [9]. An effective carrier lifetime τ_j for n$^+$-p junction can be defined as $\tau j=2C_jR_j=\frac{2Rd1Rd2}{Rd1+Rd2}(Cd1+Cd2)$. As per this equation under high FB where $C_{d1}\gg C_{d2}$ and $R_{d2}\gg R_{d1}$, τ_j is approximately equal to $2R_{d1}C_{d1}$.

In the low FB a higher and saturated value of C_j is shown and it is same as discussed by Bisquert et al. [31,51]. In the mid bias region, both base and SCR recombination dominates and hence the net recombination process is most efficient [52]. In this probed bias region a valley is observed owing to the efficient charge annihilation. The authors have explained this phenomenon by coupling the SCR and base recombination mechanism. Under high FB, τ_j increases with the increasing V_j by following the trend of C_j and can be explained on the basis of injection dependent variation of carrier lifetime.

4.2. Resistive and capacitive components of p-p$^+$ junction

The resistive and capacitive component of p-p$^+$ junction plays a crucial role in dictating the charge transport and back surface field strength at the Al back contact [53]. It is to be mentioned here that the parameters associated with p-p$^+$ junction cannot be resolved by using conventional DC characterization technique. The influence of illumination, temperature and applied bias on the parameters of p-p$^+$ junction was studied in depth by Crain et al. [9]. Fig. 15 shows the variation of R_{LH} and C_{LH} as a function of illumination and junction voltage (V_j).

The values of R_{LH} and C_{LH} have been associated with p-p$^+$ junction of a solar cell. The authors have discussed the following observation with respect to Fig.15 in support of making this attribution. In the same way as discussed for R_j and C_j plot of n$^+$-p junction, R_{LH} and C_{LH} also varies in a coupled mode with mutually opposite trend. This signifies that both these elements are associated with the single component of a solar cell. Along with the above observation, the foremost common feature of R_{LH} and C_{LH} that link these elements with p-p$^+$ junction of the solar cell are the voltage at which they are detected. At a bias below the
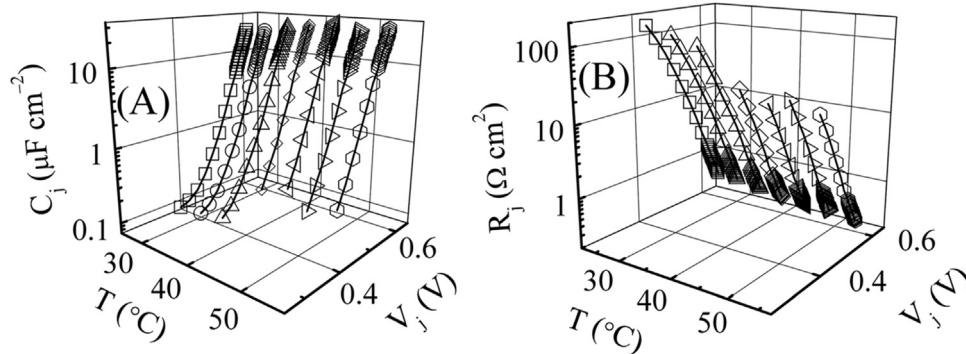

Fig. 14. (A) Capacitance, C_j, and (B) resistance, R_j, of the n$^+$-p diode junction of the Si solar cell, plotted as functions of temperature and forward bias junction voltages. [9].Reproduced from [9] with permission of The Royal Society of Chemistry.
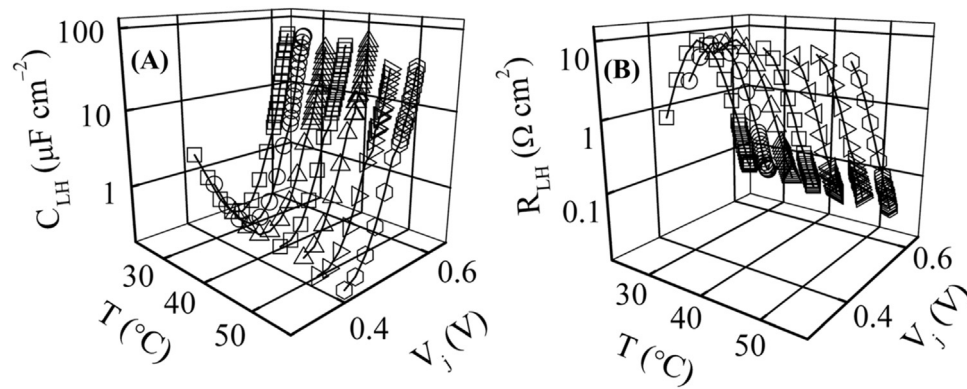
Fig. 15. (A) Temperature and forward bias dependent capacitance, C_{LH}, and (B) resistance R_{LH} of the low-high junction of the BSF solar cell [9]. Reproduced from [9] with permission of The Royal Society of Chemistry.

knee voltage, n$^+$-p junction of a solar cell works into the high impedance charge depletion mode. On the other hand, p-p$^+$ junction operate under the diffusion controlled mode where it cannot develop a complete charge depletion layer. Consequently at low FB, a higher value of R_j is accompanied by a larger reactance of C_j, whereas the impedance of p-p$^+$ junction does not change to such a large extent. This explains that why the signature of p-p$^+$ junction is not detectable under the low and moderate RB conditions. Another predictable feature of p-p$^+$ junction that is noted in Fig.15 by Crain et al. [9] is the mutually overlaying appearance of the plot collected at different illumination intensities. With the variations in the value of J, V_j also changes which changes V_{LH} simultaneously, due to the series connection of V_j and V_{LH} source diodes. Thus, rescaling of voltage from V to V_j normalizes the corresponding change in p-p$^+$ junction potential. The most noticeable finding in Fig. 15 B is that in the entire bias region, V_{LH} is less than the upper limit of the value $K_BT/|e|=26mV$, which is a distinct attribute of a typical p-p$^+$ junction. The restriction on the upper value of V_{LH} can be explained by the fact that the hole depletion layer in p$^+$ side of the p-p$^+$ junction is considerably thin than the hole accumulation layer. As a result, the built in potential (V_{P0}) of a typical p-p$^+$ junction never exceeds the value of $K_BT/|e|$ and V_{LH} which would always be less than V_{P0} remains confined below this limit [54]. At the knee voltage of a solar cell, the plot of V_{LH} for different light intensities follows the same trend with a difference in their absolute value. The authors have coupled the peak like feature observed in Fig. 15B with the peak observed in voltage dependent R_S plot. Most probably the variation in V_{LH} is caused by the Fermi level degeneracy of p$^+$-Al back contact which is turn causes the voltage dependent peak in R_S[55,56]. Such an effect could be explained by interplay between the charge transport characteristics of the BSF and those of Al back contact [8]. In the bias range beyond the knee voltage or at high FB, the value of R_{LH} is relatively small and it allows the approximate ohmic form of $V_{LH}=J'_dR_{LH}\approx J_dR_{LH}$. In this probed bias region, the parameters associated with the p-p$^+$ junction overlays in a similar fashion as of n$^+$-p junction. The values of R_{LH},C_{LH} and characteristic time constant (τ_{LH}) measured by IS as a function of voltage and temperature are shown is Fig. 16 .

The authors have given the following explanations to show that the observed characteristic time constant (τ_{LH}) is correlated with the relaxation time of the hole and not the electrons. First, the injected electrons in the base enters the LH region and the lifetime of such electrons would typically have values that are atleast an order of magnitude less than those of τ_{LH} as shown in Fig.16C [8]. Therefore, the observed value of τ_{LH} cannot be correlated with the electron recombination. The observed phenomenon regarding the correlation of τ_{LH} with hole relaxation time can be further enumerated by comparing the temperature dependence of τ_{LH} at a fixed bias with the corresponding τ_j at the same applied bias. Fig. 16C shows a $\tau_{LH}-T$ plot for V_j=0.56V and is compared to the plot of τ_j-T shown in Fig. 8 of Ref. [9]. The graph of

$\tau_{LH}-T$ deviated noticeably from the characteristic linear behaviour of τ_j over the same temperature and the probed bias. The $\tau_{LH}-T$ plot exhibits an exponential characteristic. The largely decoupled temperature dependency of τ_j and τ_{LH} supports that these observed parameters are originated from two different mechanisms. The voltage dependence of τ_{LH} can be understood by the voltage dependence term of C_{LH} and R_{LH} which is represented by $C_{LH}=(dQ_{LH}/dV_{LH})$ and $R_{LH}=(dJ/dV_{LH})$. In dark condition under the FB, the net charge Q_{LH} has the form of $|e|P_p^{LH}$ where P_p^{LH} denotes the total hole concentration in p-p$^+$ region. Thus both the terms of τ_{LH} i.e. R_{LH} and C_{LH} have voltage dependence. Therefore τ_{LH} should vary with V_{LH}. Nevertheless in the high FB region V_{LH} and V_j follows a linear relation as shown in Fig. 8B of Ref. [9]. Based on this linear relation it is possible to conclude that under high FB the voltage dependence of τ_{LH} becomes predominately exponential similar to that of τ_j.

Moreover, various methods have been employed to determine the ac parameters of solar cells using impedance spectroscopy. Chenvidhya et al. [57] developed a new method to determine the ac parameters of solar cells by doing the measurements dark conditions using square wave signal, instead of the ac sinusoidal signal. The dynamic impedance of the solar cell can be then be determined using the FFT technique and the output response. The measurement period required is smaller than the one for the impedance spectroscopy with ac sinusoidal signal because the impedance locus is obtained using few square wave inputs. Twarowski and Albrecht used the low frequency oscillographic methods to determine directly the capacitance of a solar cell [58]. In this method, an ac sinusoidal or triangular wave signal can be applied. The amplitude and the frequency of the signal can be chosen. Mandal e al. determine the capacitance using low sinusoidal wave signal of desired amplitude for the GaAs/Ge and Si (BSFR-back surface field and reflector) photovoltaic cells [59]. Kumar et al. developed a method to determine the ac parameters of solar cells using the time domain technique [60,61]. The measurements made in dark conditions consists of applying a constant current in the solar cell, equal with the short circuit current which charges the junction capacitance around the open circuit voltage.

4.3. Application of IS in silicon solar production line

The key features responsible for the discrepancies in the performance of silicon solar cells fabricated from the same ingot under the identical conditions have been thoroughly investigated by using DC and AC characterization techniques by Yadav et al. [62]. Fig. 17 shows the top view and cross sectional FESEM images of the fabricated solar cells. The deep cone shaped holes and impurity precipitates on the top surface of cells are shown by the marked regions in Fig.17 A and C respectively. The top view of both the solar cells shows an inhomogeneously distributed oval shape pits with an average grain size of few micrometres. The cross-section image (Fig.18) shows the active layer
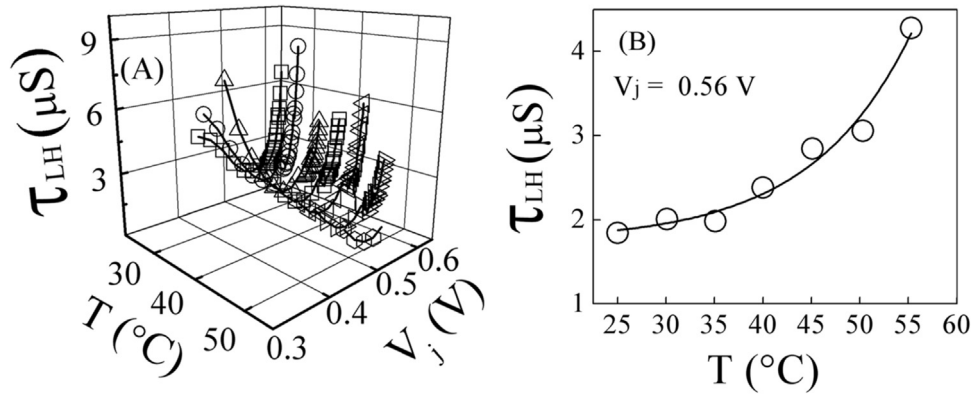
Fig. 16. (A) Relaxation time, τ_{LH}, of hole-carriers at the p-p$^+$ low-high junction of the experimental Si solar cell, determined in the absence of illumination as functions of T and forward biased V_j and (B) Functional form of the temperature dependence of τ_{LH}, examined at a high FB voltage, 0.56 V. [9]."Reproduced from [9] with permission of The Royal Society of Chemistry

thickness of ~177, ~170 and ~176 μm for cell 1, cell 2 and cell 3, respectively. The finger heights of the three cells are ~23.6, ~25.4 and ~16.6 μm, respectively whereas the respective fingers widths are ~50, ~57.5 and ~51.5 μm. The J-V characteristics and the key parameters of the solar cell i.e. V_{OC}, J_{SC}, FF,η, series resistance (R_S), etc. under 1 sun illumination (AM 1.5 1000 W/m^2) are listed and shown in Table 1 and Fig. 19 respectively.

It has been well known for single crystalline (c-Si) and mc-Si solar cells that the losses near the knee voltage are mainly influenced by R_S which are associated with the charge transfer resistance in active layer (n$^+$, p, p$^+$ layer) and contact resistance between active layer and charge extraction terminals. Also, the losses close to V_{OC} are mainly depen-

dent on the recombination kinetics [14,15].

The authors considered the net terminal J-V equation discussed in Scheme 1 to get an insight into the resistive and recombination losses [8,12,16]. By taking the derivative with respect to the net terminal voltage [12,16], one obtains $dV/dJ = R_S + m_{eff} K_B T / e [1/(J_{SC} - J)]$.

Under the RB or moderate FB condition, $eV_j / m_{eff} K_B T \gg 1$, SCR is sufficiently extended for charge separation, and R_{SH} and diode ideality factor m_2 mainly dominates the resistive and recombination losses [17].

The value of m_{eff} as a function of applied bias was also used as an indicator of the n$^+$-p junction quality. Fig. 20 shows the variation of m_{eff} as a function of n$^+$-p junction voltage for the three cells calculated using the coupled defect model after Breitenstein et al. [20]. The value of m_{eff}
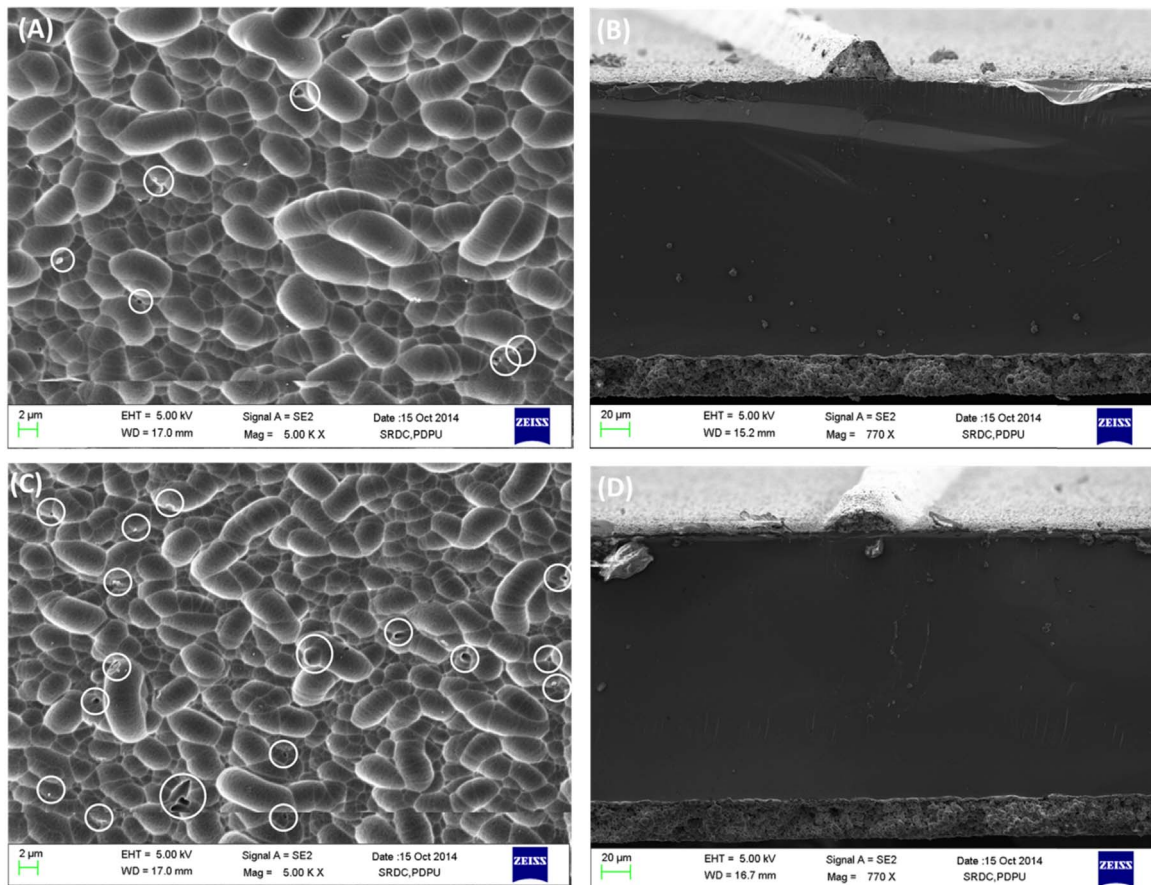

Fig. 17. SEM images of: (A) Topography of the fabricated Si solar cell 1, (B) cross-section of the fabricated Si solar cell 1, (C) Topography of the fabricated Si solar cell 3, (D) cross-section of the fabricated Si solar cell 3. [3].Reproduced from [3] with permission of Elsevier.
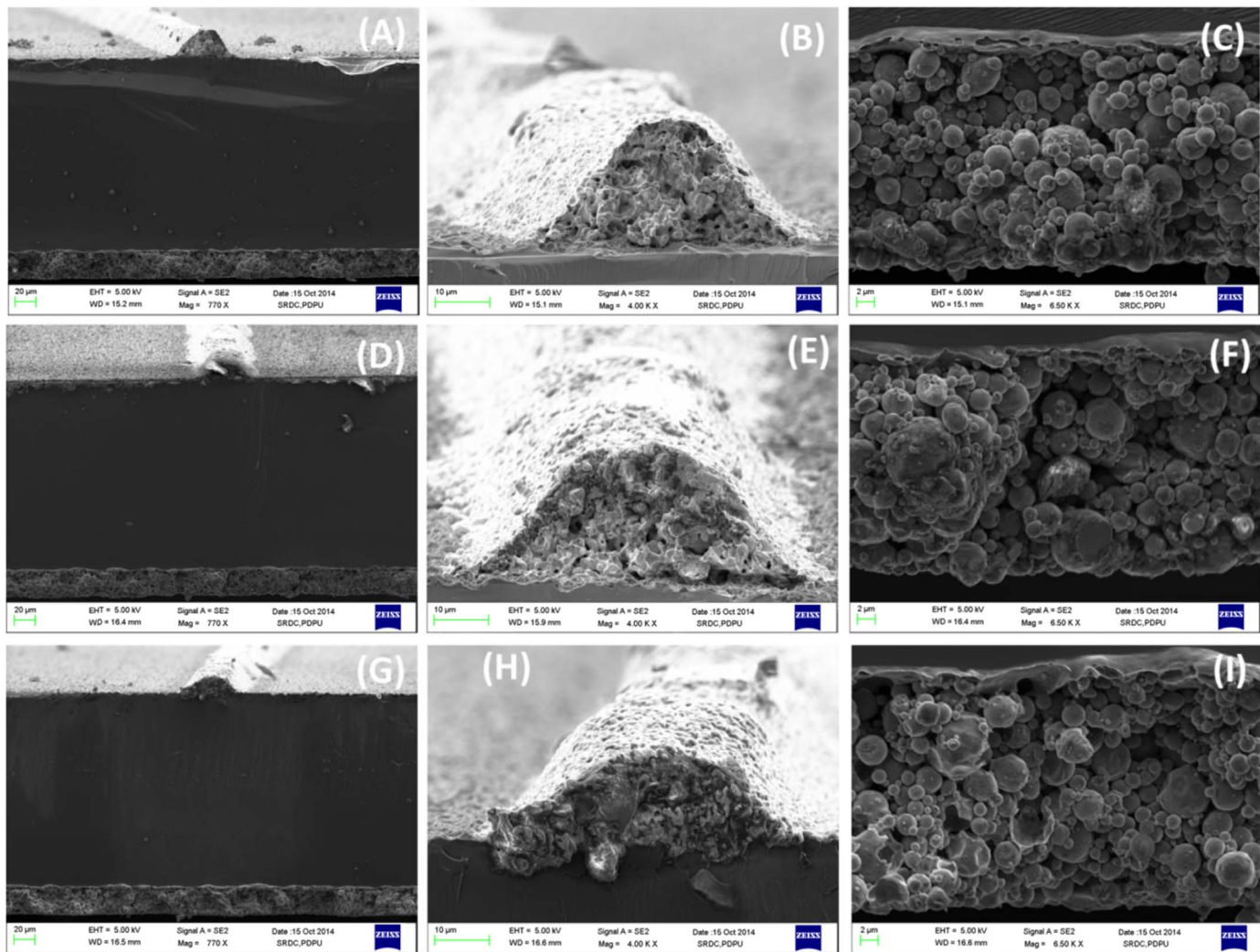
Fig. 18. SEM image of cell 1 (A) Cross-sectional view (B) enlarged view of a current-carrying finger (C) enlarged view of a back surface field layer. SEM image of cell 2 (D) Cross-sectional view (E) enlarged view of a current-carrying finger (F) enlarged view of a back surface field layer. SEM image of cell 3 (G) Cross-sectional view (H) enlarged view of a current-carrying finger, (I) enlarged view of a back surface field layer. [3].Reproduced from [3] with permission of Elsevier.

Table 1
Parameters of the multi-crystalline silicon solar cells extracted from DC characterization technique.

Parameter (Unit)	Cell 1	Cell 2	Cell 3
J_{SC} (mA cm^{-2})	38.4	38.2	38.1
V_{OC} (V)	0.6	0.59	0.58
FF (%)	77	75	72
η (%)	17.56	16.8	16
R_S (Ω cm^2)	0.80	0.92	1.49
P_{max} (mW cm^{-2})	17.5	16.8	16
V_{mp} (V)	0.49	0.48	0.47
V_{bi} (V)	0.67	0.66	0.64

Fig. 19. Current-voltage characteristics of Si solar cells manufactured in the production line [3].Reproduced from [3] with permission of Elsevier.

at ~0.3 V is equal to 3 and 8 in the case of most and least efficient cells respectively. The value of $m_{eff}>3$ over an extended voltage region is generally observed for industrial Si solar cells [20,22].

Models such as single trap level assisted tunnelling [23], field enhanced recombination [24], two level traps assisted tunnelling [25] and resistance limited recombination [22] have been used to explain the value of $m_{eff}>2$ by other researchers. The resistance limited recombination model describes some of the practical situations that explain the reason for $m_{eff}>2$ in the extended FB region [26]. Furthermore, the value of $m_{eff}>5$ signifies high density of electrically active defect states at grain boundaries [22,25]. It is well known that
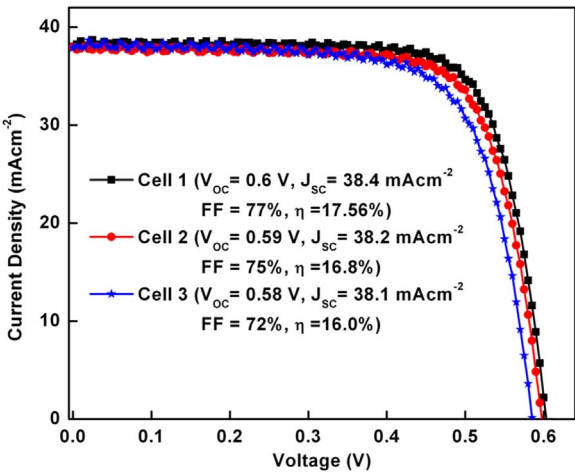
coupled defects are generally activated for defect energy levels present in the forbidden band gap which typically lies above 0.25 eV from the intrinsic Fermi level [27]. On the other hand, the value of $m_{eff}<2$ signifies the recombination of charge carriers due to the diffusion in QNR.
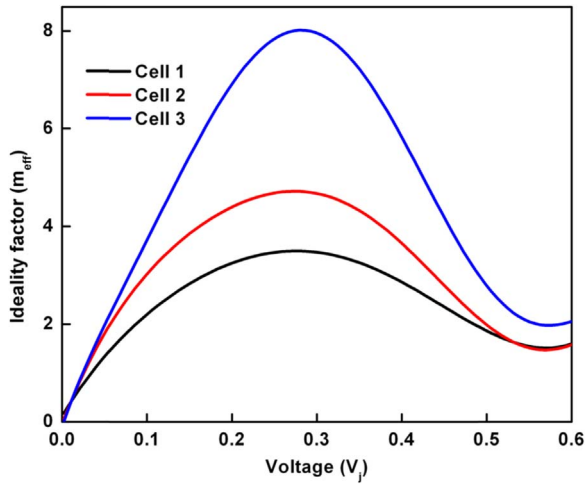
Fig. 20. Effective diode ideality factor as a function of junction voltage [3].Reproduced from [3] with permission of Elsevier.

The most prominent defects responsible for the high value of m_{eff} are the scratches, deep cone shaped holes over the surface and non-passivated edges that cross the p-n junction [22,24,63]. By comparing the surface structure of all the solar cells (Fig. 17), a higher density of impurity precipitation over grain edges and deep cone shaped holes on the surface of cell 3 grown during the acid texturing process can increase the recombination current and the values of m_{eff} [20,22,63,64]. Moreover, Yadav et al. [23] have also concluded that

besides the morphological effect, recombination current and m_{eff} is also influenced by the parameters like temperature and illumination. These authors have also employed IS technique to decouple the various photovoltaic parameters associated with the several physical processes in terms of resistive and capacitive elements [7–9] (Fig. 21).

Fig. 22A and B shows the plot of resistive and capacitive parameters as a function of V_j. The lower R_{SH} in cell 3 results in a lower FF due to the lateral drift of current and non-uniform shunts across the n+-p junction [19,20,22]. Fig. 22 B shows that all the solar cells have similar value of C_T which corresponds to the dielectric polarization originated due to the voltage modulation of depletion zone at n+-p junction. From the estimated value of $C_T=(\varepsilon e N_A/(2V_{bi} - V_j)^{0.5})$, built-in potential ($V_{bi}$) and doping concentration (N_A) can be determined using the Mott-Schottky plot from the intercept $[2V_{bi}/(q\varepsilon N_A)]$ and slope $[2/(q\varepsilon N_A)]$ of $1/C_T^2$ versus bias plot. The average value of N_A obtained for cell 1, cell 2 and cell 3 are 1.20×10^{16}, 1.23×10^{16} and 1.41×10^{16} cm^{-3} respectively and the corresponding built-in potential are 0.67, 0.66 and 0.64 V respectively. Yadav et al. [23] have shown that both the resistances R_{SH} and R_S contributes to the total resistive loss of the solar cell.

Beyond the knee voltage i.e. under high FB condition, $R_d/R_{SH} \ll 1$ and the diffusion resistance (R_d) and corresponding diffusion capacitance (C_d) dominates the total resistance of the solar cell. An exponential behaviour of R_d at high FB for all the solar cells was accounted by the following expression,

$$\ln R_d=\ln(L_n^2/(2D_n\gamma))-|e|V_j/m_1k_BT \qquad (37)$$

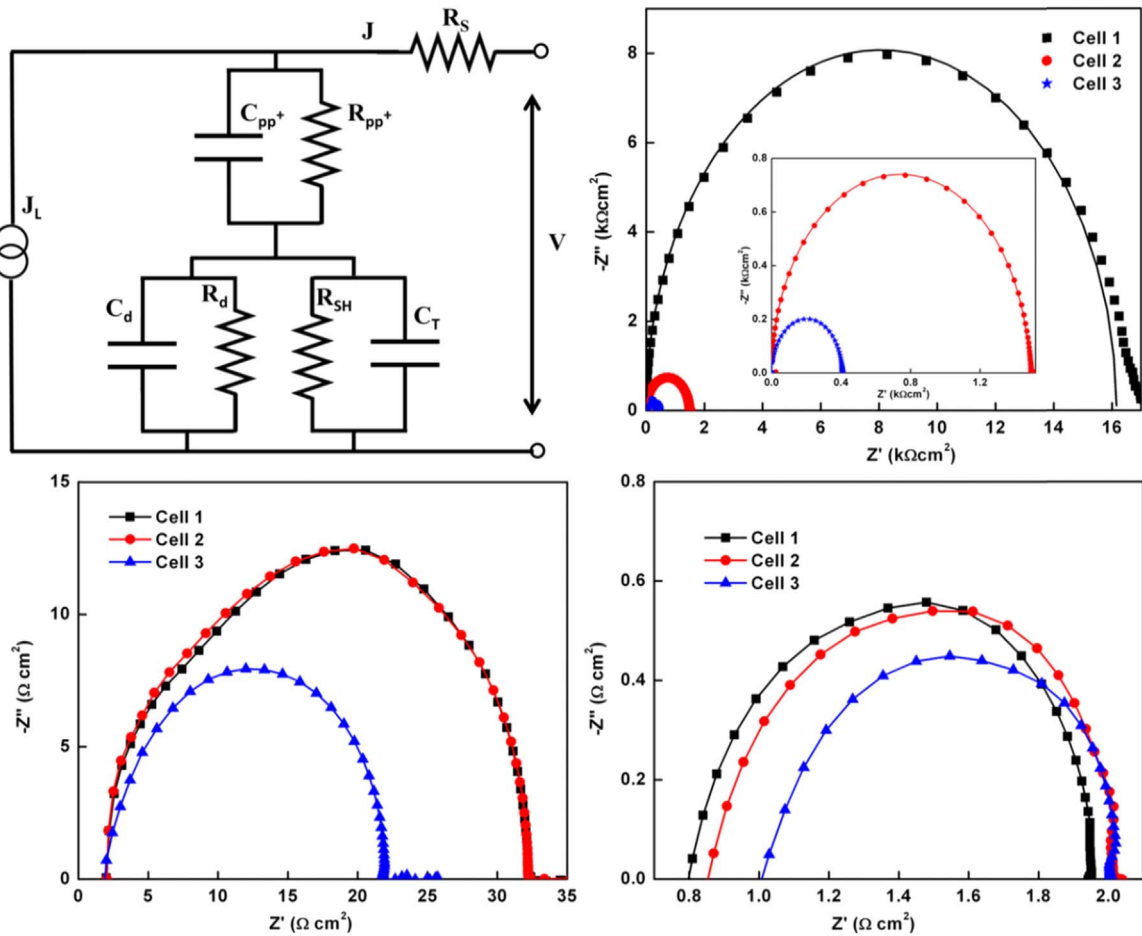where, $\gamma =[(|e|\tau_{np}J_0)/(2m_1K_BT)]$. The value of m_1 was correlated with the

Fig. 21. (A) Electrical equivalent circuit employed for fitting the impedance spectra. Impedance spectra obtained for cell 1, cell 2 and cell 3 at (B) zero bias, (C) knee voltage of the corresponding solar cells and (D) open circuit voltage of the solar cells. The inset in Fig. 21B shows the magnified view of $Z'vs.Z'$ for cell 2 and cell 3 at zero bias. [3].Reproduced from [3] with permission of Elsevier.
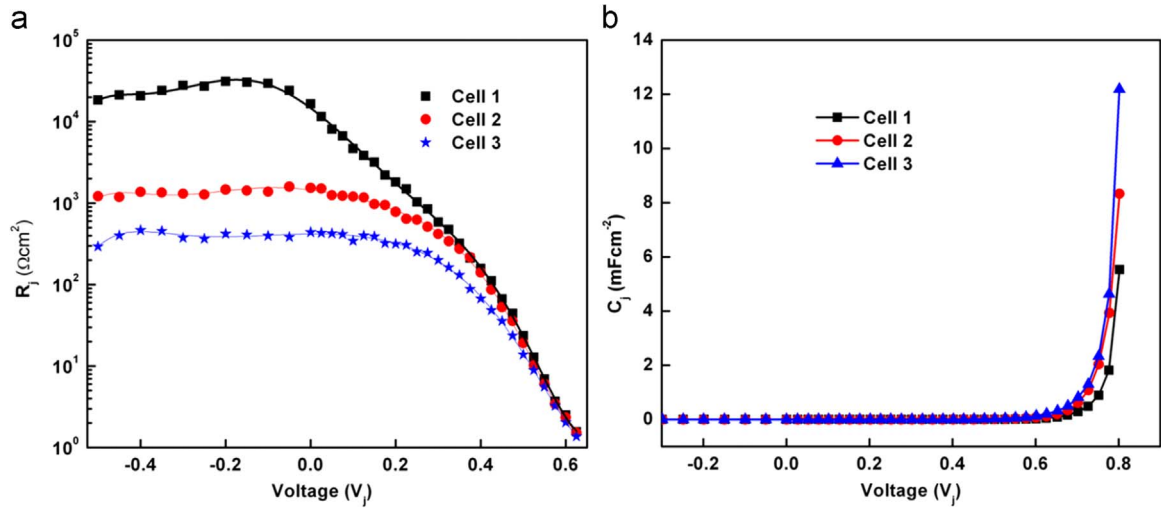
Fig. 22. Variation of (A) Resistance and (B) Capacitance at n+-p junction as a function of junction voltage. [3].Reproduced from [3] with permission of Elsevier.

recombination coefficient β as $\beta = 1/m_1$ by the authors, where β is in the range of $0 < \beta < 1$. The diode ideality factor in terms of β could be determined from the slope of linear region of $\ln R_d$ versus V_j plot. The lower value of β signifies the presence of non-linear recombination process mediated by surface states that limits the performance of a solar cell. Guillén et al. [65] have explained that the recombination taking place via charge transfer is responsible for a lower value of β.

Figs. 23 and 24 show the variation of relaxation time associated with the n+-p junction of the solar cell as a function of junction voltage. It was presumed by the authors that the value of τ_{n+p} and its trend depends on the several interfacial phenomena; (i) distance between n+-p junction and BSF, (ii) presence of BSF, and (iii) dependence of the values of R_j and C_j on V_j. It was inferred from an almost same value of R_{pp+} that equal series resistance is faced by the charge carriers. In the low FB region, a comparatively lower value of τ_{n+p} for cell 3 is due to the relatively lower R_{SH} associated with n+-p shunt type defects. Breitenstein et al. and other authors [20,22,64] have associated these shunt type defects to the defect density, energy level coupling, n+-p junction states, and bulk and surface recombination.

Under the high FB condition, i.e. beyond the knee voltage, the recombination in bulk region dominates and τ_{n+p} increases with V_j by largely following the voltage dependence of C_j. Hence, by discarding the processes (i), (ii) and recombination in bulk as discussed by Yadav et al. [62], the limiting factors for low τ_{n+p} are the surface recombination and impact of R_{SH}. The key features responsible for the discrepancies in the performance of silicon solar cells fabricated from the same ingot under
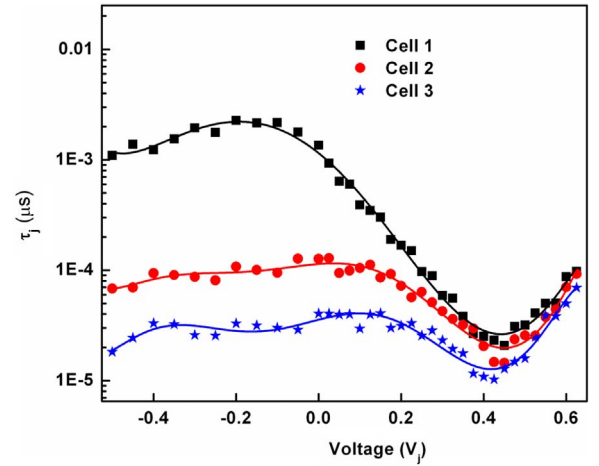
the identical conditions have been thoroughly investigated by Yadav et al. [62]. The higher density of deep cone shaped holes and impurity precipitates in cell 3 as compared to that of cell 1 is assumed to be one of the possible reasons for the difference in performance of solar cells by these authors. The higher resistive and recombination losses have seen to be dominate the performance of least efficient solar cell. Under
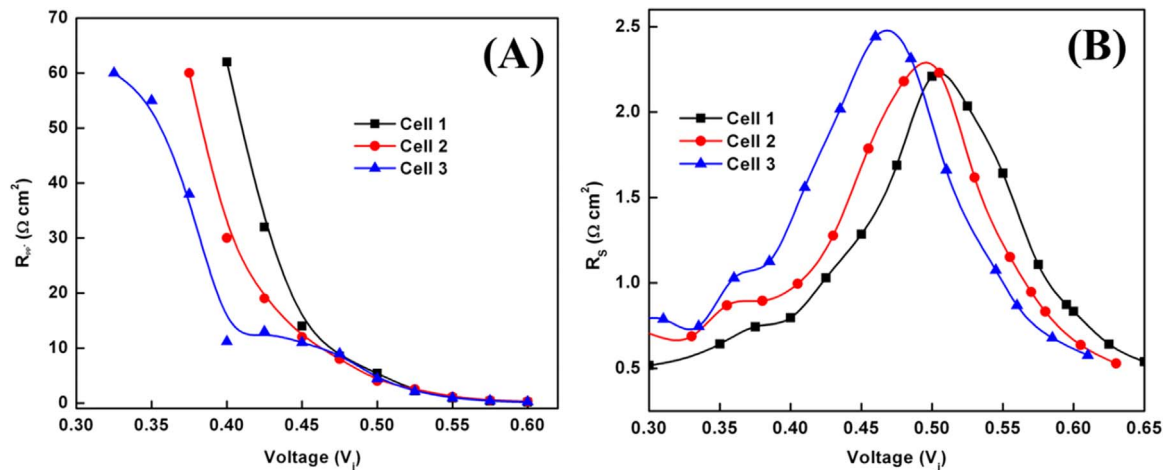

Fig. 24. Variation of minority carrier lifetime at n+-p junction of the solar cell. [3].Reproduced from [3] with permission of Elsevier.

Fig. 23. Variation of (A) Resistance at p-p+ junction and (B) non-ohmic series resistance as a function of junction voltage. [3].Reproduced from [3] with permission of Elsevier.

moderate RB or at 0 V, all the solar cells exhibit maximum impedance and follow the description of a single time constant. Thus, the results reported by Yadav et al. [54] can be used as a simple tool that can be integrated with the conventional photovoltaic testing.

5. Future aspects of IS measurement

Impedance spectroscopy is a single-sine method in which a small ac wave of 5–15 mV of a given frequency is overlaid on a desired dc bias potential and applied to the working electrode; an ac current measurement is then made. This process is repeated by scanning the frequency and computing the impedances from the ac voltage and current data at desired frequencies, typically five to ten measurements for a decade change in frequency. However, this method is viable only for a stable and reversible system in equilibrium, as the system's linearity, stability, and causality must be ensured. For this reason, early investigators questioned the validity of impedance measurements [66,67] and hoped to make instantaneous impedance measurements for nonstationary systems. Stoynov & Savova-Stoynov [68–71] published mathematical expressions to extract instantaneous impedance values for nonstationary systems. Problems with this approach arise primarily from the relatively long data-acquisition time required for the single-sine impedance method.

In efforts to reduce the measurement time, investigators have proposed methods in which no frequency scanning is employed. Smith [72] and others [73–75] used the fast Fourier transform (FFT) method after obtaining the current signal upon application of a noise signal, which was achieved by mixing the ac voltages of various frequencies, to an electrochemical cell. Recently, Popkirov and Schindler [76] simplified this technique and implemented it into an EIS spectrometer through use of a noise signal obtained by mixing the ac waves of 42 appropriate frequencies.

Park et al. [77,78] demonstrated that their FTEIS technique can serve as a more sensitive time-resolved detection tool than can its voltammetric counterpart for biosensors. Darowicki & Slepski [79] examined the well-known electrochemical reaction involving reduction of Cd^{2+} at a hanging mercury electrode, and they characterized the reaction in terms of R_p and C_d, along with Warburg coefficients, as a function of reduction potential. The new FTEIS techniques are expected to elucidate various unsolved problems in electrochemistry.

Novel experiments that were thought to be difficult, if not impossible, to perform without the new FTEIS techniques should be explored in order to solve complex problems encountered during the studies on electrochemical energy conversion, biosensors, and other materials-related areas.

6. Conclusions

This review, in detail, assess and discusses the various impedance models developed to characterize a silicon solar cell. This review presents a complete overview of the various mathematical models to analyse the experimental impedance spectroscopic data for interfacial processes of a silicon solar cell. The most suitable model can be chosen to analyse the silicon solar cell or the other new types of solar cell. However, care must be taken while choosing the appropriate model to avoid the errors in fitting the impedance spectra. Moreover, the experimental procedure to be employed for error free measurements is also briefly discussed. The discussion is mostly based on elucidating the recombination and resistive losses in the solar cells, decoupling various photovoltaic parameters associated with different physical processes in terms of its resistive and capacitive elements and analysis of relaxation time associated with the solar cells. These performance indicating parameters are mostly characterized by DC techniques, where it is difficult to get some information about some important parameters such as interfacial diffusion and transition capacitance, and resistive and capacitive components of p-p$^+$ interface of a silicon solar cell. Thus, the understanding of the experimental results along with the appropriate analytical model can be used as a simple tool to characterize a solar cell and it can be integrated with the conventional photovoltaic testing.

Appendix A

Notations	Definitions
V_T	thermal voltage
$m1$	ideality factor
L_n	electron diffusion length
$n\text{po}$	electron concentration
$\varphi(x)$	potential profile at LH interface
p^+	acceptor concentration
J'_d	current through LH junction
J_d	current through the diode current
$R\text{s}$	series resistance
J_0	reverse saturation current
J_{0b}	contribution from base saturation current
J_{0e}	contribution from emitter saturation current
R_d	diffusion resistance of the n$^+$-p junction
C_d	diffusion capacitance
J_{db}	base component of diode's diffusion current
J_{de}	emitter component of diode's diffusion current
J_{d1}	current through diode 1

J_{d2}	current through diode 2
m_1	diode ideality factor of diode 1
m_2	diode ideality factor of diode 2
R_r	resistance of charge recombination in SCR
C_r	capacitance of charge recombination in SCR
ω_d	effective rate constant of diffusion in a finite layer
ω	angular frequency
D_n	electron diffusion co-efficient
ω_{rec}	recombination characteristic frequency
L_n	electron diffusion length
L	active layer thickness
C_μ	chemical capacitance
n_0	minority charge carrier in equilibrium
α	contributions from trap level

References

[1] Basore PA. Proceedings of the 4th IEEE world conference on photovoltaic energy conversion (WCPEC'07). vol. 2; 2007. p. 2089–93.
[2] Yadav P, Tripathi B, Pandey K, Kumar M. Sol Energy Mater Sol Cells 2015;133:105–12.
[3] Yadav P, Pandey K, Tripathi B, Kumar CM, Srivastava SK, Singh PK, Kumar M. Sol Energy 2015;122:1–10.
[4] Lee E, Lee H, Choi J, Oh D, Shim J, Cho K, Kim J, Lee S, Hallam B, Wenham SR, Lee H. Sol Energy Mater Sol Cells 2011;95:3592–5.
[5] Yin WW, Wang XS, Zhang F, Zhang LJ. IEEE. J Photovolt 2013;3:697–701.
[6] Zhao J, Wang A, Green MA, Ferrazza F. Appl Phys Lett 1998;73:1991–3.
[7] Garland JE, Crain DJ, Roy D. Sol Energy 2011;85:2912–23.
[8] Garland JE, Crain DJ, Zheng JP, Sulyma CM, Roy D. Energy Environ Sci 2011;4:485–98.
[9] Crain DJ, Garland JE, Rock SE, Roy D. Anal Methods 2012;4:106–17.
[10] Crain DJ, Rock SE, Garland JE, Roy D. Curr Appl Phys 2013;13:2087–97.
[11] Mora-Seró I, Garcia-Belmonte G, Boix PP, Vazquez MA, Bisquert J. Energy Environ Sci 2009;2:678–86.
[12] Santiago FF, Bisquert J, Palomares E, Otero L, Kuang D, Zakeeruddin SM, Gratzel M. J Phys Chem C 2007;111:6550–60.
[13] Garcia-Belmonte G, Guerrero A, Bisquert J. J Phys Chem Lett 2013;4:877–86.
[14] Fabregat-Santiago F, Bisquert J, Garcia-Belmonte G, Boschloo G, Hagfeldt A. Sol Energy Mater Sol Cells 2005;87:117.
[15] Wang Q, Moser J-E, Graetzel M. J Phys Chem B 2005;109:14945.
[16] Bisquert J, Garcia-Belmonte G, Munar A, Sessolo M, Soriano A, Bolink HJ. Chem Phys Lett 2008;465:57.
[17] Crain DJ, Zheng JP, Roy D. Solid State Ion 2013;240:10–8.
[18] Zheng JP, Moganty SS, Goonetilleke PC, Baltus RE, Roy D. J Phys Chem C 2011;115:7527–75372.
[19] Bayhan H, Kavasoglu AS. Sol Energy 2000;361:303.
[20] Proskuryakov YY, Durose K, Taele BM, Oelting S. J Appl Phys 2007;102:024504.
[21] Anil-Kumar R, Suresh MS, Nagaraju J. Sol Energy 2004;76:417.
[22] Raniero L, Fortunato E, Ferreira I, Martins R. J Non-Cryst Solids 2006;352:1880.
[23] Yadav P, Tripathi B, Pandey K, Kumar M. Phys Chem Chem Phys 2014;16:15469.
[24] Nelson J. The physics of solar cells. London: Imperial College Press; 2004.
[25] Goetzberger A, Knobloch J, Voss B. Crystalline Silicon Solar Cells. New York: J. Wiley; 1998.
[26] Singh SN, Singh PK. IEEE Trans Electron Devices 1991;38:337–43.
[27] Morales-Acevedo A, Santana G, Martel A, Hernandez L. Solid-State Electron 1999;43:2075–9.
[28] Thongpron J, Kirtikar K, Jivacatea C. Sol Energy Mater Sol Cells 2006;90:3078–84.
[29] Garland JE. Ph.D. Thesis. Clarkson University; 2011.
[30] Kumar RA, Suresh MS, Nagaraju J. Rev Sci Instrum 2001;72:3422–6.
[31] Bisquert J, Mora-Seró I, Fabregat-Santiago F. Chem Electro Chem 2014;1:289–96.
[32] Ding D, Johnson SR, Yu SQ, Wu SN, Zhang YH. J Appl Phys 2011;110:123104.
[33] Kumar S, Singh PK, Chilana GS. Sol Energy Mater Sol Cells 2009;93:1881–4.
[34] Kumar S, Srivastava R, Chilana GS, Singh PK. J Optoelectron Adv Mater 2007;9:371–4.
[35] Singh PK, Kumar R, Vinod PN, Chakravarty BC, Singh SN. Sol Energy Mater Sol Cells 2003;80:21–31.
[36] Thouti E, Komarala VK. Sol Energy 2016;132:143–9.
[37] Bisquert J. Phys Chem Chem Phys 2003;5:5360.
[38] Mora-Seró I, Luo Y, Garcia-Belmonte G, Bisquert J, Muñoz D, Voz C, Puigdollers J, Alcubilla R. Sol Energy Mater Sol Cells 2008;92:505.
[39] Raniero L, Fortunato E, Ferreira I, Martins R. J Non-Cryst Solids 2006;352:1880–3.
[40] Berry WB. Appl Phys Lett 1974;25:195–6.
[41] Moore AR. RCA Rev 1975;36:551–65.
[42] Moore AR. Appl Phys Lett 1975;27:26–9.
[43] Araujo GL, Sancez E. IEEE Trans Electron Devices 1982;29:1511–3.
[44] Cotfas DT, Cotfas PA, Kaplanis S. Renew Sustain Energy Rev 2016;61:213–21.
[45] Green MA, Blakers AW, Zhao J, Milne AM, Wang A, Dai X. IEEE Trans Electron Devices 1990;37:331–6.
[46] Glunz SW, Nekarda J, Mäckel H, Cuevas A. Proceedings of the 22nd European photovoltaic solar energy conference. Milan (Italy); 3–7 September, 2007. p. 849–53.
[47] Adegboyega GA, Poggi A, Susi E, Castaldini A, Cavallini A. Appl Phys A: Mater Sci Process 1989;48:391–5.
[48] Schroder D, Meier DL. IEEE Trans Electron Devices 1984;31:637–47.
[49] Conley JW, Duke CB, Mahan GD, Tiemann JJ. Phys Rev 1966;150:466–9.
[50] Raniero L, Fortunato E, Ferreira I, Martins R. J Non-Cryst Solids 2006;352:1880–3.
[51] Bisquert J, Garcia-Canadas J, Mora-Seró I, Palomares E. Organic photovoltaics IV. Proceedings of SPIE, 5215. Bellingham, WA: SPIE; 2004. p. 49–59.
[52] Garland JE, Pettit CM, Roy D. Electrochim Acta 2004;49:2623–35.
[53] Orazem ME, Tribollet B. Electrochemical Impedance Spectroscopy. Hoboken: Wiley; 2008.
[54] Fossum JG. IEEE Trans Electron Devices 1977;24:322–5.
[55] Sharma AK, Singh SN, Bisht NS, Kandpal HC, Khan ZH. Sol Energy Mater Sol Cells 2012;100:48–52.
[56] Drummond P, Kshirsagar A, Ruzyllo J. Solid-State Electron 2011;55:29–36.
[57] Chenvidhya D, Kirtikar K, Jivacate C. Sol Energy Mater Sol Cells 2003;80:459–64.
[58] Twarowski AJ, Albrecht AC. J Chem Phys 1979;70:2255–61.
[59] Mandal H, Saha S. An improved technique of capacitance measurement of solar cells. In: Proceedings of the third international conference on computer, communication, control and information technology (C3IT), Hooghly, India; 2015.
[60] Kumar RA, Suresh MS, Nagaraju J. Rev Sci Instrum 2003;74:3516.
[61] Deshmukh MP, Kumar RA, Nagarajua J. Rev Sci Instrum 2004;75:2732–5.
[62] Yadav P, Pandey K, Tripathi B, Kumar M. Sol Energy 2015;116:293–302.
[63] Li SS. Semiconductor physical electronics. New York: Plenum Press; 1993.
[64] Streetman BG. Solid state electronic devices. Englewood Cliffs: Prentice Hall; 1995.
[65] Sze SM. Physics of semiconductor devices. New York: J. Wiley; 1981.
[66] Sluyters-Rehbach M, Sluyters JH. J Electroanal Chem 1979;102:415–9.
[67] Popkirov GS, Schneider RN. Electrochim Acta 1993;38:861–7.
[68] Stoynov ZB, Savova-Stoynov BS. J Electroanal Chem 1985;183:133–44.
[69] Savova-Stoynov BS, Stoynov ZB. Electrochim Acta 1992;37:2353–5.
[70] Stoynov Z. Electrochim Acta 1992;37:2357–9.
[71] Stoynov Z. Electrochim Acta 1993;38:1919–22.
[72] Smith DE. Anal Chem 1976;48:A221–A240.
[73] Jeno H, Elton DM, Czerwinski WA, Schiewe JG, Vicente-Beckett VA, Bond AM. J Electroanal Chem 1997;437:1–15.
[74] Uhlken J, Waser R, Wiese H. Phys Chem 1988;92:730–5.
[75] Hazı J, Elton DM, Czerwinski WA, Schiewe JG, Vicente-Beckett VA, Bond AM. J Electroanal Chem 1997;437:1–15.
[76] Popkirov GS, Schindler RN. Rev Sci Instrum 1992;63:5366–72.
[77] Park JY, Lee YS, Chang BY, Karthikeyan S, Kim KS, et al. Anal Chem 2009;81:3843–50.
[78] Park JY, Chang BY, Nam H, Park SM. Anal Chem 2008;80:8035–44.
[79] Darowicki K, Slepski P. J Electroanal Chem 2003;547:1–8.